This document has been reviewed and determined not to contain export controlled technical data.

Casey Seyb – April 1, 2020

National Aeronautics and Space Administration

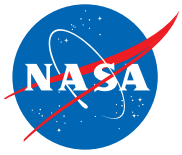

JPL D-26533

Earth Observing System (EOS)
Aura Spacecraft

TROPOSPHERIC EMISSION SPECTROMETER (TES)

Instrument Calibration Report

Volume 1

Preliminary Version

September 26, 2003

JPL D-26533

TROPOSPHERIC EMISSION SPECTROMETER (TES)

Instrument Calibration Report

Reinhard Beer	Jet Propulsion Laboratory
Kevin W. Bowman	Jet Propulsion Laboratory
Brendan M. Fisher	Jet Propulsion Laboratory
Michael R. Gunson	Jet Propulsion Laboratory
Ron G. Holm	Jet Propulsion Laboratory
Mingzhao Luo	Jet Propulsion Laboratory
David M. Rider	Jet Propulsion Laboratory
Edwin Sarkissian	Jet Propulsion Laboratory
Susan Sund Kulawik	Jet Propulsion Laboratory
Denis A. Tremblay	Raytheon
Helen M. Worden	Jet Propulsion Laboratory

Approved by: _____

Reinhard Beer, TES Principal Investigator

_____

Thomas A. Glavich, TES Project Magnager

Preliminary Version
September 26, 2003

The research was carried out at the Jet Propulsion Laboratory, California Institute of Technology, under a contract with the National Aeronautics and Space Administration (80NM0018D0004).

TABLE OF CONTENTS

Volume 1

Volume 2

1. RELEVANT DOCUMENTS

Tropospheric Emission Spectrometer: Science Objectives & Approach, Goals & Requirements. JPL D-11294, Version 6.0, April 1999.

Tropospheric Emission Spectrometer: Instrument Pre-Flight Calibration Requirements. JPL D-20040, Version 1.2, February 9, 2003.

Tropospheric Emission Spectrometer: Spectrometer Instrument Calibration Plan. JPL D-13432,1996.

Tropospheric Emission Spectrometer:Integration and Test Plan. JPL D-15389,2000.

Tropospheric Emission Spectrometer: Level 1B Algorithm Theoretical Bases Document. JPL D-16479, Version 1.1, October 1999.

Tropospheric Emission Spectrometer: Level 2 Algorithm Theoretical Bases Document. JPL D-16474, Version 1.1, October 1999.

2. CALIBRATION REQUIREMENTS SUMMARY

Detailed calibration requirements are given in *Tropospheric Emission Spectrometer: Instrument Pre-Flight Calibration Requirements*. JPL D-20040, Version 1.2, February 9, 2003. We summarize them below, under the categories: radiometric, spectral and spatial.

Radiometric Calibration

Measurements taken for radiometric calibration must be sufficient to determine instrument response linearity, radiometric accuracy, specified in equivalent brightness temperature and precision, specified as the noise equivalent spectral radiance (NESR) over the expected range of source temperatures, with calibration sources that are traceable to NIST radiance standards. There is also a requirement to calibrate relative gain settings in the signal chain; however, this has very low priority since we do not plan to exercise the different settings at this time.

Spectral Calibration

Spectral calibration results must characterize spectral response and stability, frequency positions of spectral lines with respect to known line positions (e.g., the HITRAN database) and the instrument line shape (ILS).

Spatial Calibration

Spatial calibration measurements must provide the field of view (FOV) response function for each detector at each filter setting, along with the relative co-boresight for the four focal plane arrays at a spatial resolution sufficient for accurate radiance models in the limb view. In addition, co-boresight measurements from the on-board spatial calibration source (OBSCS) must be verified using the external spatial calibration source (target projector). Finally, the pointing control system (PCS) must be calibrated with respect to the TES and Aura spacecraft alignment reference cubes.

3. SYSTEM TESTING BACKGROUND

4. TEST CONFIGURATIONS

The characterization measurements of the TES instrument are performed in the same thermal environment that is expected on orbit. Eight temperature control zones provide the means for simulating the on-orbit thermal environment. Seven of these zones supply gaseous or liquid nitrogen to thermal panels and test equipment. The eighth thermal zone is supplied with helium. Six thermal shrouds are provided within the system; each is independently supported from the chamber through thermal insulators and is independent of the vibration-isolated optical bench. The operational temperature range of the chamber is from 220 to 280 K. It operates with an active load of 350 W and a maximum temperature gradient of 16 K. Figure 4.1 presents the layout, within the thermal vacuum chamber, of the TES instrument and its calibration equipment.

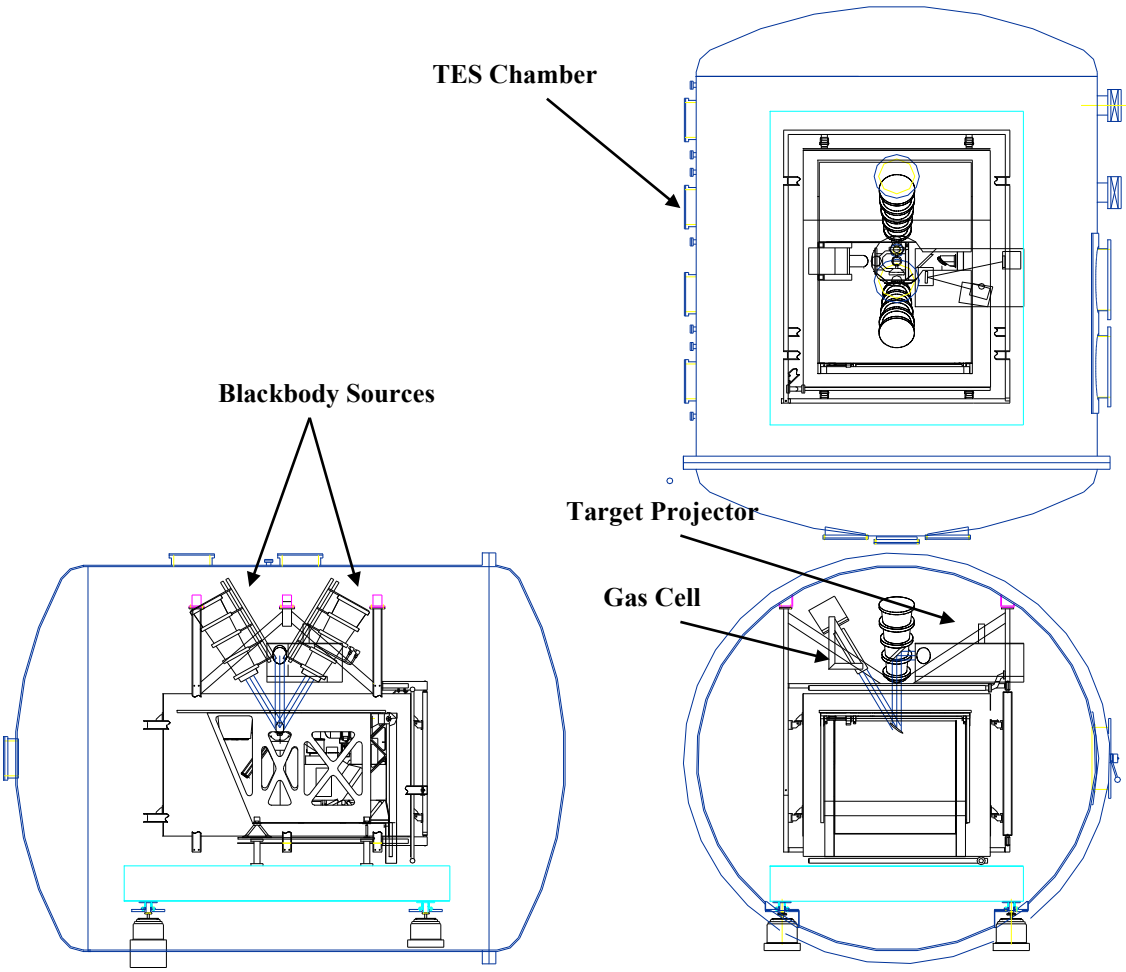

Figure 4.1. Thermal Vacuum Chamber Layout

Radiometric Test Sources

The radiometric calibration of the instrument is performed using two thermally controlled, high-emissivity blackbody sources. Each blackbody source is mounted inside the chamber in direct view of the instrument. There are no additional optics placed between the instrument and the calibration sources. One blackbody source is cooled with LN_2 to approximately 80 K to simulate the view of cold space. The second blackbody is a variable-temperature source (Figure 4.2) that operates between approximately 90 and 350 K. The effective temperature of the sources is controlled using heater elements and LN_2 cooling. The temperature is monitored using readings from calibrated PRT temperature sensors placed on the source.

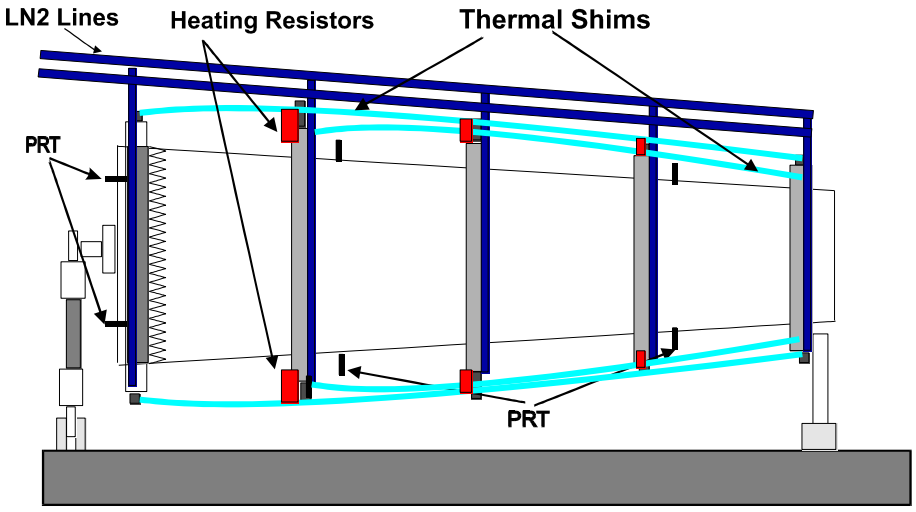

Figure 4.2. Variable Temperature Blackbody Layout

Spatial Calibration Source

Field-of-view (FOV) and spatial characterization tests are performed using a vacuum-qualified target projector. This projector (Figure 4.3) consists of a high-temperature infrared source (uncalibrated), off-axis collimator, chopper (operating at 80 Hz), and a set of interchangeable apertures on a computer-controlled X-Y stage. The IR-illuminated aperture of the target projector is positioned at the focus of an off-axis paraboloid and imaged by the TES instrument onto its detectors. A remotely controlled translational stage scans the illuminated aperture across the FOV of the instrument.

The instrument views the target projector via the TES PCS mirror. Mechanical stability is provided by mounting the target projector on a vibration-isolated optical table.

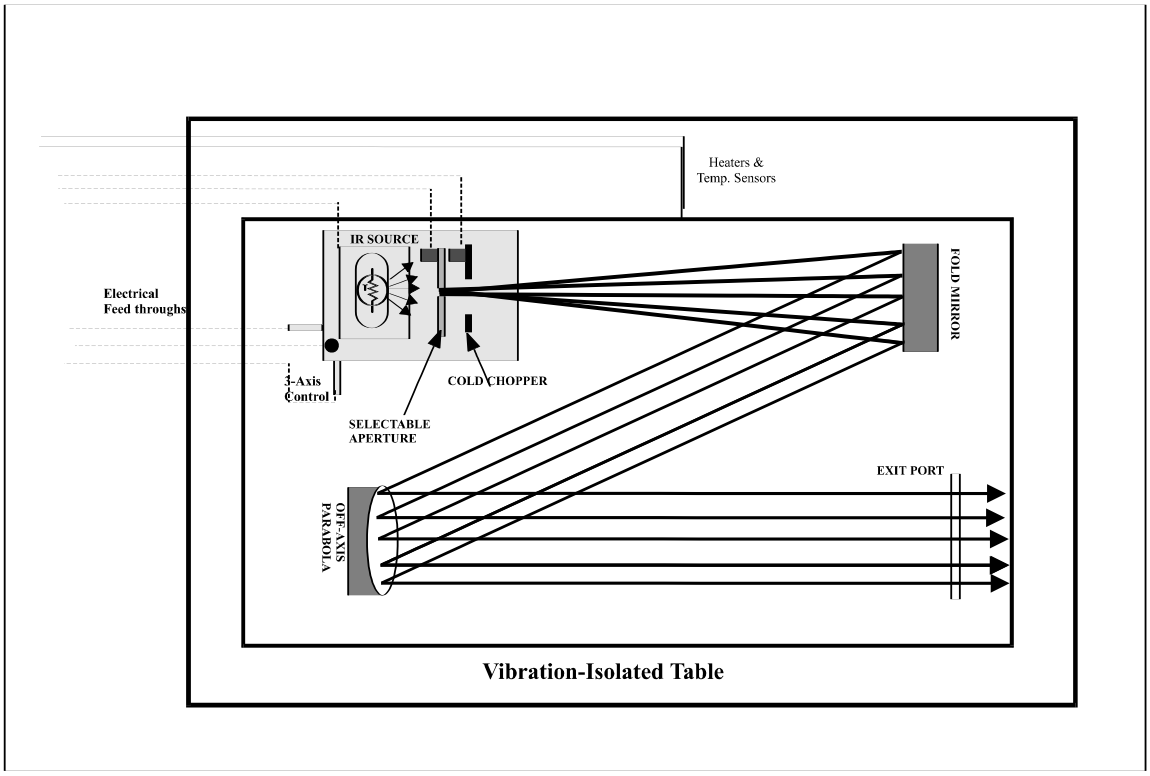

Figure 4.3. TES Target Projector

Spectral Calibration Sources

The spectral calibration of the instrument is measured by comparing recorded spectra of a gas cell (Figure 4.4) filled with a known gas, at a known temperature and pressure, with the spectral line widths of reference test gases. To avoid the strong pressure-broadened water vapor lines that occur in the atmosphere, all spectral measurements are taken in the evacuated chamber with a pressure of $<10^{-5}$ torr. The gas cell is a cylinder with a 40-cm path length and a 13.25-cm IR transmitting window. A stable large-area (20-by-20-cm) blackbody source operating at 340 K provides the input radiance used to illuminate the gas cell. Temperature sensors placed on the external surface of the cell provide the temperature monitoring required to accurately predict the line widths of the gas under test. The gas cell has two input lines that interface with chamber feedthroughs and connect to a manifold outside the chamber. The manifold provides the input port and purge line for the test gases and performs the monitoring and control of the pressure within the cell.

A second spectral measurement is performed using a stable monochromatic source. This measurement provides a single-frequency measurement of the instrument line shape and provides a validation of the gas-cell measurements. Spectra are recorded while viewing the monochromatic source, which illuminates the instrument through an IR-transmitting window placed in one of the chamber viewing ports.

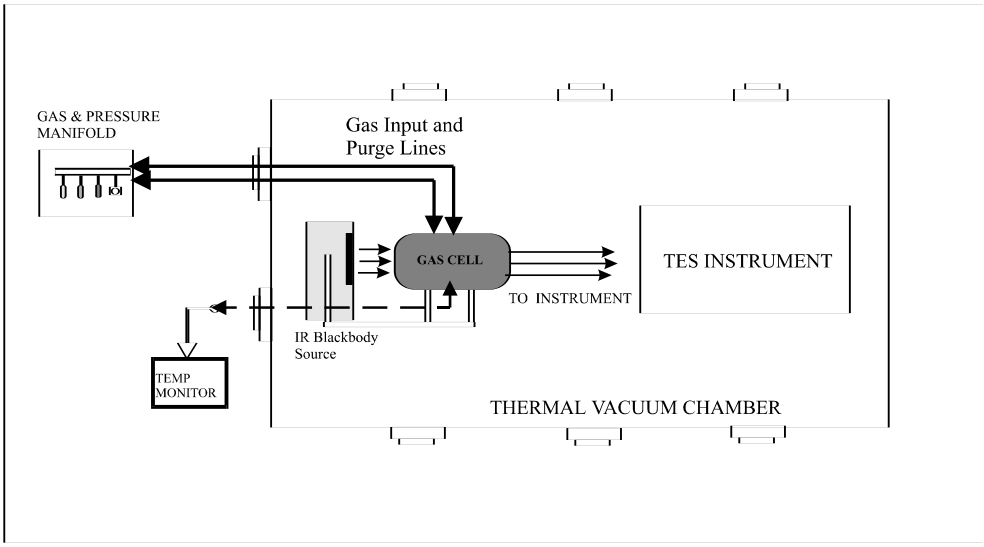

Figure 4.4. TES Spectral Calibration Source

5. KEY DATA SUMMARY

Radiometric Calibration and NESR

Primary dataset: ST-5 runs 504-515 (testIDs 416-427) with external variable blackbody at 120K to 340K, 20K increments. This dataset used the same gain settings for data taken from the external variable blackbody, the OBRCS and the external cold (90K) blackbody.

Secondary dataset: ST-5 runs 447-449,453-460, (testIDs 358-360,364-371) with external variable blackbody at 120K to 340K, 20K increments. This dataset also used different gain settings for the external blackbody as temperature was varied. Data from the OBRCS view were always taken with a low gain setting and data from the external cold (90K) blackbody were always taken with the highest gain settings.

Spectral Calibration

CO_2 Laser: ST-5 run 498 (testID 410). TES was illuminated with scattered light from a CO_2 laser. Such a device emits many lines but the ones used in this study were the two strongest: P20 at 1046.8543 cm^{-1} and R24 at 1081.0877 cm^{-1}, both from the 00^01-02^00 band. TES filters 1B1 and 1B2 cover the CO_2 lines.

Gas Cell: ST-5A runs 461-473 (testIDs 372-384) and ST-5B runs 516-529 (testIDs 428-441). The gas cells include CO2 at 150 and 10 Torr respectively, N2O at 150 and 5 Torr respectively, and CO at 5 Torr. The gas cell temperatures were at room temperature, about 290 K. The blackbody background temperatures for the gas cell measurements were all set to 340 K. For a given gas cell measurement, two empty cell measurements were taken before and after, with 340 K and 320 K blackbody background temperatures respectively. The OBRCS and Cold BB measurements are also taken.

Spatial Calibration

The spatial calibration data was taken for FOV response and co-boresight. For each testid/runid, there were 200 scan steps, with one scan per step.

Set Number	TestIDs[1]	RunIDs[1]	Filters	Notes
1	354, 355, 356	443,444,445	1A1,1B1,2A1,2B1	Missed detectors
2	385,386,387	474,475,467	1A1,1B1,2A1,2B1	Filter set 1
3	392	481	1A1,1B1,2A1,2B1	Out of field, above
4	393	482	1A1,1B1,2A1,2B1	Out of field, below
5	395,396,398	484,485,487	1A2,1B2,2A2,2B1	Filter set 2
6	400,401,402	489,490,491	1A3,1B1,2A3,2B1	Filter set 3
7	404,405,406	493,494,495	1A4,1B1,2A4,2B1	Filter set 4
8	442,442,444	530,531,532	1A1,1B1,2A1,2B1	Filter set 1
9	447	535	1A1,1B1,2A1,2B1	Out of Field, above
10	448	536	1A1,1B1,2A1,2B1	Out of Field, below
11	450,451,452	538,539,540	1A2,1B2,2A2,2B1	Filter set 2
12	454,455,456	542,547,548	1A3,1B1,2A3,2B1	Filter set 3
13	458,459,460	546,547,548	1A4,1B1,2A4,2B1	Filter set 4
14	527,528,529	634,635,636	1A1,1B1,2A1,2B1	Filter set 1
15	541,542,543	648,649,650	1A1,1B1,2A1,2B1	Filter set 1

[1] ID numbers are for along track, cross track top, and cross track bottom sets

The FOV data used for the level 2 OSP were set 2 for filters 1A1, 1B1, 2A1, 2B1, set 5 for filters 1A2,1B2,2A2, set 6 for filters 1A3 and 2A3, and set 7 for filters 1A4 and 2A4. The co-boresight fot the OSP was derived from set 15. Set 13 is contaminated with interferogram spikes.

6. CALIBRATION RESULTS SUMMARY

The following 16 sections briefly summarize the analysis results on the TES calibration data. More detailed analyses can be found from the JPL internal memorandums in Volume 2 of this report.

6.1 Channel Shifts

Background

In ST-1, incorrect assignments of pixel were first observed in data from the target projector. The data was processed using the known channel-to-pixel map from the hardware specifications. Since the target projector scans across the detector arrays, if the channel assignment has been shifted during the data collection, the incorrect pixel order is obvious. Since then, other methods to detect channel shifts have been discovered that do not require target projector data and channel shifts in the data have been observed throughout the system testing with relatively high occurrence, on average, around 1 shift per run.

If there is any mis-timing in the real-time interrupts sent to the signal chain MUX (multiplexer), the channel being read can jump to another channel. Following a flight software fix after ST-1, this only happens at the beginning of scans. Since channel number is inferred by the order of the interferogram samples, with no other ancillary identification, the apparent channel order is shifted when this occurs. To arrive at the correct assignment of pixel, the interferogram array must be shifted back to the correct order, removing the possible junk in the first interferogram sample from each channel before the channel shift occurred. The mapping from channel to pixel can then be applied.

Hardware channel maps:

	1A, 2A arrays	
	pix 15	-ch 00
ch 08-	pix 14	
	pix 13	-ch 01
ch 09-	pix 12	
	pix 11	-ch 02
ch 10-	pix 10	
	pix 09	-ch 03
ch 11-	pix 08	
	pix 07	-ch 04
ch 12-	pix 06	
	pix 05	-ch 05
ch 13-	pix 04	
	pix 03	-ch 06
ch 14-	pix 02	
	pix 01	-ch 07
ch 15-	pix 00	

	1B, 2B arrays	
	pix 15	-ch 08
ch 00-	pix 14	
	pix 13	-ch 09
ch 01-	pix 12	
	pix 11	-ch 10
ch 02-	pix 10	
	pix 09	-ch 11
ch 03-	pix 08	
	pix 07	-ch 12
ch 04-	pix 06	
	pix 05	-ch 13
ch 05-	pix 04	
	pix 03	-ch 14
ch 06-	pix 02	
	pix 01	-ch 15
ch 07-	pix 00	

Channel shift detection and correction

The two methods that have been used for channel shift detection are summarized as

1) Interferogram mean value. This method makes use of a fortuitous artifact of the signal chain. Due to differences in biasing resistors, all the detectors have slightly different interferogram mean values after A-D conversion. These mean values provide a 16-element array for each detector array that can be used for correlation with the mean interferogram values from each scan. A channel shift is observed as a shift in channel position for the peak correlation.

2) Non-linear behavior in slope of zpd offset vs. pixel. If pixels were not correctly assigned, the pattern of zero-path-difference (zpd) offsets, which should fall on a straight line as a function of pixel becomes obviously distorted. This method cannot be used if the spectral phase is indeterminate, i.e., when the signal is too low.

The correct assignment of pixel is critical for both L1B and L2 processing. Therefore, the channel shift correction requires a robust method that can detect a channel shift from any scan, regardless of the target source. The current processing approach applies the first method, using interferogram mean values to detect channel shifts and apply the corrections in L1A. The correction of the channel shift is verified in L1B for OBRCS (340K) calibration spectra when the interferometer shear is computed, which uses the slope of zpd offsets and checks for linearity vs. pixel.

Channel Shift DFMs:

TES A&S DFM # 435, “Absolute channel mean value map”, R. Beer, 4/23/2003.
TES A&S DFM # 443, “Phase analysis approach to shear estimation”, K. Bowman, E. Sarkissian, 5/1/2003.
TES A&S DFM # 445, “Validation of channel shift detection using interferogram mean value map”, H. Worden, K. Fry, 5/6/2003.
TES A&S DFM # 493, “Correcting interferogram sample timing to account for channel shifts”, E. Sarkissian, H. Worden, 8/10/2003.

6.2 FFT Size / Filter Spectral Range

FFT Size Determination

Raw interferograms are truncated to a prime-factor FFT size that allows efficient computing. The FFT size determines the spectral resolution used for processing the calibration data taken during the System Test 5 (ST5). It will be used for the operational level 1B calibration processing.

The interferogram Zero Path Difference (ZPD) corresponds to the maximum deviation from the mean. Taking a symmetric number of data points about the ZPD index and truncating it to the next smaller prime-factor number gives a good FFT size. The determination of the operational FFT size is based on the statistical distribution of two sided interferogram size with a centered ZPD index.

A total of 89,079 interferograms taken during ST5 were processed. For example, Figure 6.2.1 shows the half size of the two sided interferogram for the clock divisor value 9 and for low resolution scans. For this case, the FFT size half is found to be 16200. The long scan FFT size will be 4 times larger. Table 6.2.1 shows the FFT size results.

Table 6.2.1. FFT Size of Short and Long Scans.

Divisor Clock	Short Scan	Long Scan
8	18200	72800
9	16200	64800
10	14580	58320
11	13312	53248
12	12150	48600

It was found that the smaller side of a full interferogram for a forward scan direction occurs after the ZPD index. It occurs before the ZPD index for the reverse scan direction. Referring to Figure 3, DFM 456-6.1, the ZPD index distribution is somewhat uniform outside the main cluster. For ZPD indices outside the main cluster, no correlation was found with any physical attributes (Filter, scan resolution, scan direction, scan view) suggesting it is caused by the TES instrument start scanning mechanism.

For more details, see the TES A&S DFM 456-6.1, “FFT Size Determination From ST5 Calibration Data”.

Figure 6.2.1. Histogram of interferogram ZPD indices for clock divisor value 9, low resolution scans. For this case, the FFT size half is found to be 16200.

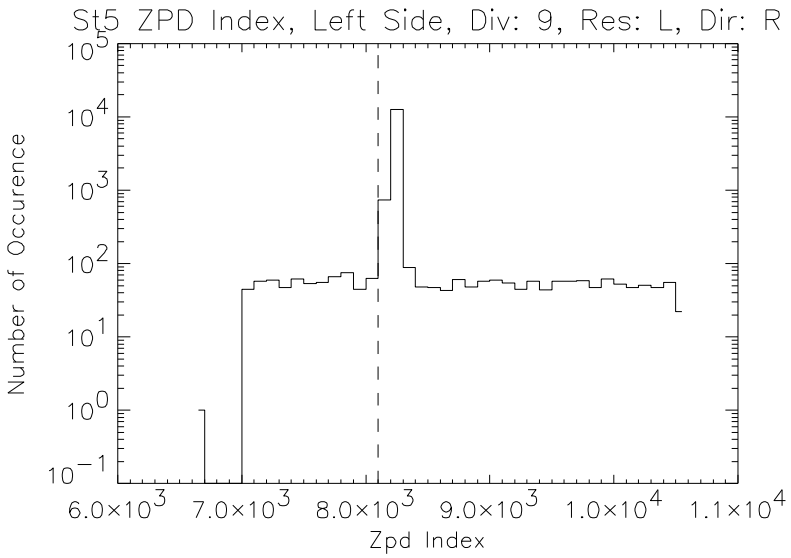

Filter Range

To the nearest 10 cm^{-1}, the filter half-power point frequency ranges observed for 340K OBRCS system test spectra are given in the following table.

TES Filter	Frequency Range (cm^{-1})	Wavelength Range (μm)
2B1	650 - 930	15.4 - 10.8
1B1	810 - 1060	12.3 - 9.4
1B2	920 - 1160	10.9 - 8.6
2A1	1090 - 1350	9.2 - 7.4
2A2	1280 - 1580	7.8 - 6.3
2A3	1480 - 1780	6.8 - 5.6
2A4	1670 - 1980	6.0 - 5.1
1A1	1890 - 2260	5.3 - 4.4
1A2	2190 - 2470	4.6 - 4.0
1A3	2410 - 2690	4.1 - 3.7
1A3	2570 - 2850	3.9 - 3.5
1A5	2750 - 3050	3.6 - 3.3

Reference with figures: TES DFM #1367.

6.3 Shear / Co-Boresight

6.4 Time Trend of Signal Level, Ice Buildup

During the TES system tests, the measured signals from the on-board radiometric calibration source (OBRCS) were used to monitor the radiometric stability of the instrument over time. The OBRCS was set to its operating temperature 340 K and the PCS track/x-track angles were kept the same through all five system tests.

The spectral magnitudes as a function of frequency derived from fixed number of interferogram points per filter/pixel are used to examine the spectral signatures, the pixel dependencies, and the time trends of the signal level. The signal levels are mainly affected by two factors, the ice/solid CO_2 buildups on the detectors and the instrument alignment.

The ice / solid CO_2 buildups on the detected had been expected. This effect dominated the downward time trends of the signal levels of filter 2B1 and 1B1 (TES DFM #1362 and DFM A&S 491). Periodically warming up of the detectors is therefore necessary though less ice is expected in space. Figures 6.4.1 and 6.4.2 below show the dominant effect of ice buildups on integrated spectral magnitudes of 2B1 and its spectral features respectively.

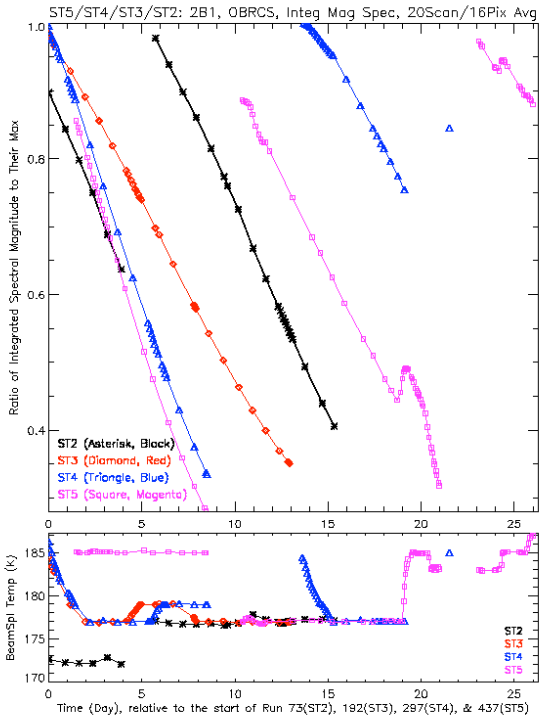

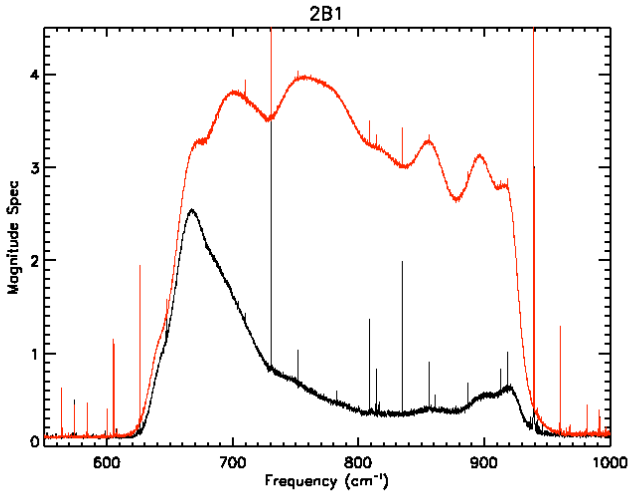

Figure 6.4.1. Integrated spectral magnitudes for 2B1 as functions of time (day) for ST2, ST3, ST4, and ST5. The beam splitter temperature time trend plot is also provided.

Figure 6.4.2. Spectral magnitudes of best (no-ice) and worst (a lot of ice and poor alignment) measurements taken in ST5.

The signal level changes with the change in the instrument alignment. This effect dominates the time trends of the signal levels of filters 2A4 and 1A1 (TES DFM A&S 491). Figure 6.4.3 and 6.4.4 below show the dominant effect of alignment on 2A4 integrated spectral magnitudes and its spectral features respectively. The signal level time trends for other filters showed the mixed effects of ice buildup and alignment. Great deals have been learned about the instrument through examining the relationships among the analyses of the shears, the co-boresights, and the time trends of the signal levels.

Keeping track of the integrated spectral magnitude is a simple way of monitoring the instrument radiometric performance. This method should be applied for on-orbit calibration data.

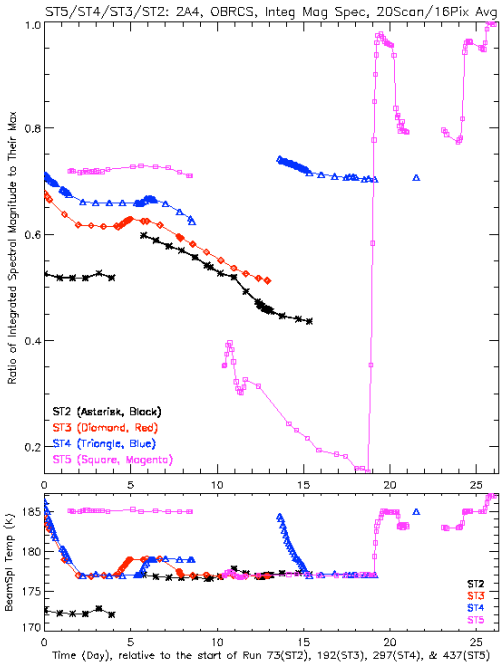

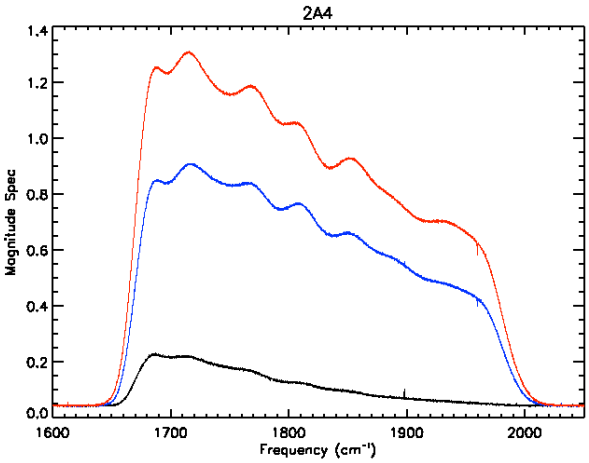

Figure 6.4.3. Integrated spectral magnitudes for 2A4 as functions of time (day) for ST2, ST3, ST4, and ST5. The beam splitter temperature time trend plot is also provided.

Figure 6.4.4. Spectral magnitudes of best (alignment), typical (alignment) and worst (alignment) measurements taken in ST5.

6.5 Channeling

Channeling is a common artifact in FTS spectra that appears as a near-sinusoidal modulation in the spectral continuum. Although wedging of optical elements can significantly minimize the effect, it is hard to eliminate altogether. However, if the channeling spectral features are stable enough, they are completely removed in the process of radiometric calibration since they are common to both target and calibration spectra. The issues that concern us for characterizing the channeling are therefore the stability of the amplitudes, frequency positions and periods of the spectral features.

Since channeling features have appeared in all system test data, it was possible to perform an analysis before ST-5. Using ST-4 data, the channeling amplitude was measured as less than 1%, as expected, and the period was greater than 1 cm^{-1} as required. An investigation of the stability of the features showed that over a 5 day period, the features are cancelled in spectral ratios. This meets the requirements for global survey calibration where calibration spectra are applied to target scans acquired within about 36 hours of the calibration scans. Channeling spectral features also had to be tested for cancellation when lower resolution (4 sec.) calibration spectra are interpolated and used to calibrate higher resolution (16 sec.) scans. In all filters, there were no residual channeling features in the differences between interpolated short scans and measured long scans.

6.6 Electrical Filter

From science test (ST) 1, it became immediately obvious that spectra measured from the on-board radiometric source (OBRCS) contained unexpected features in both the magnitude and phase when the electrical filters were turned on. In ST 4, measurements were made of the OBRCS with both the electrical filters on and off. The difference in the magnitude spectrum of the electrical filter-on case relative to the magnitude spectrum of the electrical filter-off case is over 10% at certain frequencies. Furthermore, the phase of the OBRCS measurement is non-linear with respect to frequency near the optical filter edge. As a result, the electrical filters were turned off for all subsequent ST experiments. The loss of the electrical filters resulted in a roughly factor 3 increase in signal-to-noise ratio.

The spectral distortion seen in the spectra appears to result from a subtle relationship between the electrical filters and the velocity of the interferometer relative to the analog-to-digital (A/D) samplers. The non-linear phase response of the electrical filters induced a phase dispersion in the interferogram. The non-uniform time sampling of the phase dispersion in the interferogram, which is due to the nonlinear velocity characteristics of the interferometer arm, resulted in a distorted signal. A simulation study was conducted based on this TES sampling model that produced spectral characteristics similar to those observed in ST4. A method for correcting the nonuniform velocity when the electrical filters are on was proposed in TES A&S DFM 521 given a sufficiently accurate knowledge of the velocity. However, the preliminary results have not been conclusive. Additional investigation is required.

6.7 Gain

Requirement

Each of the 64 TES signal chains has four switchable gains, nominally x0.5, x2, x8 and x32 for the "A" arrays and x0.5, x1, x2 and x8 for the "B" arrays. Since it may occur that, for example, OBCRS 340K calibrations are taken at a different gain setting from "cold space" calibrations, it is essential that the *relative* gains be known to better than 0.5%. Note that the *absolute* gains are irrelevant (because they are subsumed in the radiometric calibration process), so the lowest gain setting is arbitrarily assigned an exact value of 0.5 and the other gains determined with respect to this value.

Method

TES detectors have a "closed" filter wheel setting so that the detectors see nothing but a cavity at a temperature of about 80K(?). Measuring the gain then reduces to a measurement of the mean noise power at each setting. The exact approach is fully described in A&S DFM 436 (see Volume II).

The method determines the relative gains to a precision of 0.3% or better, so the requirement has been satisfied.

Comment

It is highly probable that we will operate TES at a constant 0.5 gain setting, thus rendering this calibration moot. Nevertheless, it will be repeated on orbit in case different gains should be re-introduced.

6.8 Spectral Spikes

The spikes appeared in nearly all processed TES spectra. These spikes were found reproducible over the system tests, *e.g.,* occurred in the same spectral frequency points for a given type of measurement (*e.g.,* global survey). The analysis of the frequencies and amplitudes points directly to electromagnetic pickup of the analog-to-digital converter-sampling clock by the signal chains.

DFM A&S 447 describes the general characteristics of the spikes, the algorithm used to identify the spikes, and the spike lists generated from global survey data taken in ST5 Part B. The products of this analysis will be used in initial Level 1B data processing for de-weighting the spectral points with spikes. Figure 6.8.1 and 6.8.2 below show two examples of the spiky magnitude spectra, 2B1 and 1B2.

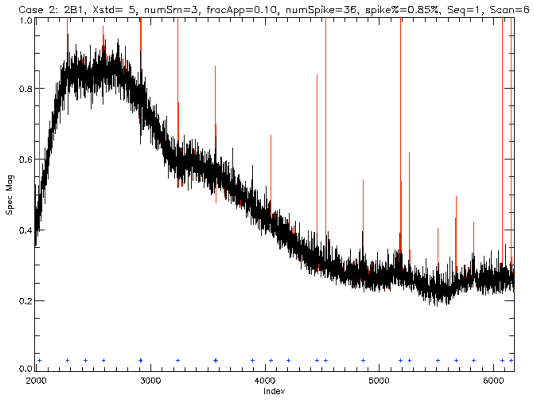

Figure 6.8.1. Illustration of spikes in magnitude spectra, 2B1, short scan.

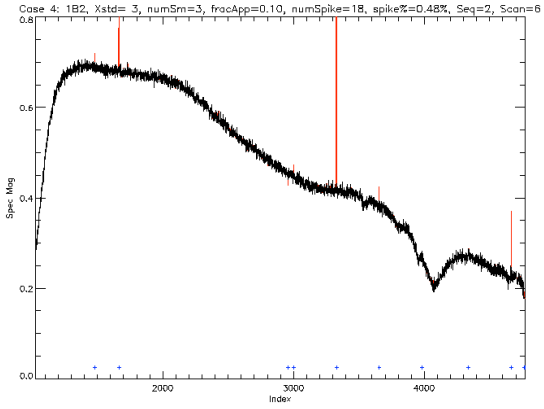

Figure 6.8.2. Illustration of spikes in magnitude spectra, 1B2, short scan.

6.9 Pointing Angles for Calibration Sources

Since an absolute calibration of the PCS (pointing control system) was not available, optimal pointing angles were determined for the on-board and external calibration sources using target search procedures designed to produce maps of source signal levels over a grid of pointing angles.

Spectral and radiometric sources

The same methods for determining the optimal pointing angles were applied for the external gas cell, external cold (90K) source, external variable blackbody and the on-board radiometric calibration source (OBRCS), *i.e.*, the internal variable blackbody. The measurements for these "target searches" were obtained by stepping through a 9 x 9 grid of track and x-track PCS angles with 2 scans at each grid point. The grids were centered on the best known angles for each source before the target search.

The data were processed by converting interferograms to magnitude spectra and performing a spectral average, after removing any spikes. It was also critical to account for channel shifts since the pixels were processed separately. Using the spectral averaged magnitude, a single values could be assigned for each pixel, each PCS angle. Contour maps of magnitude values vs. track and x-track angles showed that an adequate range of target signal levels were subtended by the grid of PCS angles.

To find the angles that produce the maximum signal levels (or minimum in the case of the external cold blackbody), we compute the angular intersection of two signal-weighted curves. For example, the values in the x-track curve are the signal-weighted x-track angles computed from each along-track cross-section. See Fig. 6.9.1 for an example. The optimal angles were reported for each focal plane, using the average over the detectors. Final PCS angle values used in ST-5 command macros were the focal plane averages.

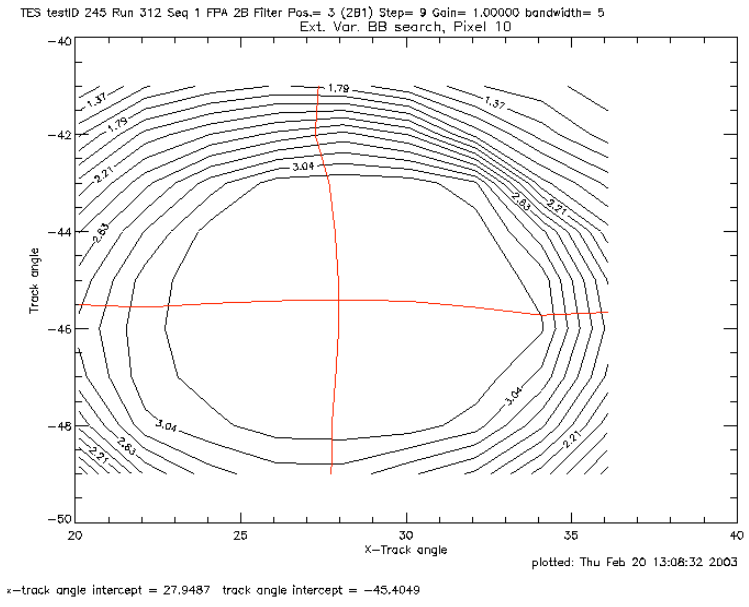

Figure 6.9.1. Example of intersecting curves used to determine pointing angles for the external calibration sources and OBRCS. The signal-weighted curves are overplotted on a contour map of signal levels for the external variable blackbody.

Reference: TES DFM # 1366, "ST-4 Target Search Results", H. Worden, 3/6/2003.

Spatial Calibration Source

The on-board spatial calibration source (SCS) was used to help validate the PCS pointing and TES absolute boresight. Additionally, it was used, and will be used on orbit, to evaluate co-boresight in the along track direction. The SCS was also used for evaluation of the jitter in the PCS system.

6.10 PCS Calibration

The TES pointing and control system (PCS) operates a two-axis gimbaled mirror, M1, that points the line of sight (LOS) of the instrument over abroad range of angles with respect to the Aura spacecraft. The objective of the PCS calibration was to determine the angular relationship between the TES line of sight and the Aura spacecraft base coordinate system for any given set of PCS gimbal angles. The final result of the calibration together with spacecraft position and attitude is used to locate TES measurements on the surface of the earth. The calibration required a number of measurements of the alignment of various elements of TES and the spacecraft. These measurements were brought together to determine the overall relationship between the LOS, the PCS gimbal encoder angles and the Aura spacecraft. A detailed description of the data and analysis is reported in DFM 1437. The material presented here provides an overview of the approach, a summary of the data and the final result.

The calibration utilized TES radiometric measurements of the TES onboard spatial calibration source (SCS) and theodolite measurements of the SCS slit and of optical alignment reference cubes, commonly referred to simply as alignment cubes, mounted on the SCS, on the instrument base structure and on the spacecraft. The radiometric measurement provided the relationship between the LOS and PCS gimbal angles. Theodolite measurements of the SCS alignment cube, the instrument alignment cube and of an alignment cube mounted on the spacecraft provided the relationship between the SCS and the Aura spacecraft base coordinate system.

LOS to SCS Slit Measurement

The SCS is a collimated slit source mounted on the interior of the TES instrument. In flight it will be used to measure the relative alignment of the four test detector arrays. However, its absolute position with respect to the instrument alignment cube is known with enough accuracy that it can also serve as a pointing reference with respect to the instrument structure. During system test 5 a series of interferograms of the SCS were recorded over a range of PCS angles. The prescribed angles were chosen to lie on lines parallel to the long axis of the detector arrays. The interferograms were converted to spectra and integrated to provide the response of the 16 pixels of the 2A detector array as a function of PCS angles. Figures 6.10.1 illustrated the PCS angles used for the measurement. Figure 6.10.2 is an example of the integrated response data.

The PCS pointing reference for the field-of-view of the instrument is defined as the midpoint of the line defined by the junction between pixels 8 and 9. The PCS angles for this point with respect to the SCS slit was determined from a two-dimensional fit to the response curves. The details of the fit are given DFM 1406. The final results are summarized in Table 6.10.1.

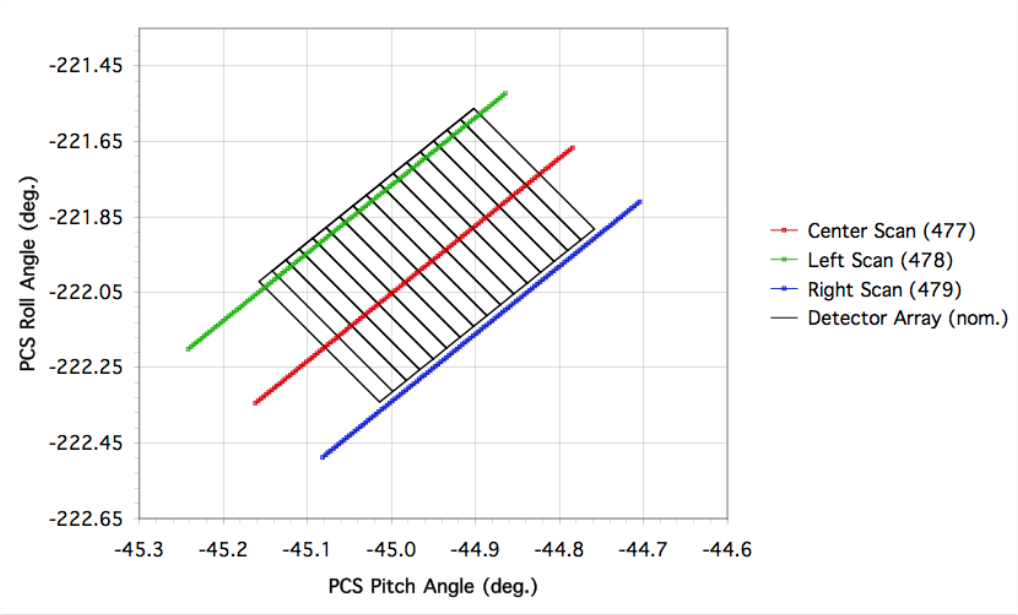

Figure 6.10.1. The PCS scan lines used to determine the instrument boresight with respect to the SCS slit. The rotated grid is represents the nominal location of a detector array. The numbers in parentheses in the legend are the run counter setting of the recorded data.

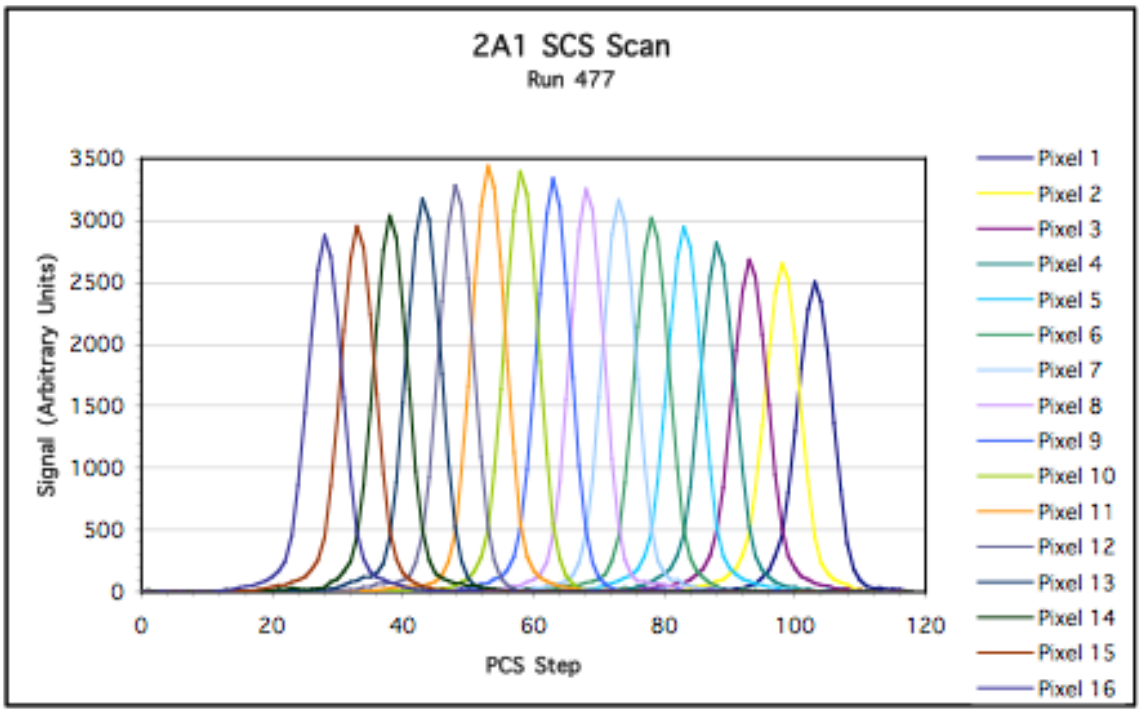

Figure 6.10.2. Example of the integrated spectra from a scan of the PCS. This is from the 2A1 detector array/filter.

Table 6.10.1. PCS angles that place the center the TES line of sight on center of the SCS slit.

PCS Gimbal	PCS Gimbal Angle (deg.)
Pitch	-44.958 ± 0.002
Roll	-221.952 ± 0.002

Alignment Cube Measurements

Of the four sets of thodolite measurements used to relate the boresight to the spacecraft coordinate system, three of the sets, the relationship of the SCS slit to the SCS alignment cube, the relationship of the SCS alignment cube to the instrument alignment cube (IAC) were made at JPL. The results, reproduced in Tables 6.10.2, 6.10.3 and 6.10.4, are reported as Euler direction cosines (unit vectors) in the instrument base coordinate system. The relationship between the instrument and the spacecraft was measured at by NGST, using the instrument alignment cube as a reference. The Euler direction cosines are given in Table 6.10.5.

Table 6.10.2. SCS slit direction cosines in the instrument coordinate system.

	Instrument X	Instrument Y	Instrument Z
SCS Slit X	0.000107294	0.642648041	-0.766161526
SCS Slit Y	-0.647484997	0.583919641	-0.489694835
SCS Slit Z	-0.762078189	-0.496025552	0.416167616

Table 6.10.3. SCS alignment cube direction cosines in the instrument base coordinate system.

	Instrument X	Instrument Y	Instrument Z
SCS Cube X Face	0.999997213	-0.000309776	-0.000689598
SCS Cube Y Face	0.000314787	0.996536593	0.083123097
SCS Cube Z Face	0.000660201	-0.083124884	0.996540199

Table 6.10.4. IAC direction cosines in the instrument base coordinate system.

	Instrument X	Instrument Y	Instrument Z
IAC X Face	0.553999774	-0.832516887	-0.000056208
IAC Y Face	0.832516871	0.553999258	0.000715970
IAC Z Face	-0.000564919	-0.000443429	0.999999714

Table 6.10.5. Spacecraft body fixed direction cosines in the TES alignment cube coordinate system. This matrix is referred to below as S.

	IAC X	IAC Y	IAC Z
S/C X	0.55428212442495	0.83232884714490	-0.00012943492856
S/C Y	-0.83232852135924	0.55428203376661	0.00081214253476
S/C Z	0.00074771311512	-0.00034242370680	0.99999966183549

Transformation of the Line of Sight in PCS angles to Spacecraft Coordinates

The direction of the line of sight after reflection by the M1 mirror is give by the rotation matrix

$$LOS_{PCS} = \begin{bmatrix} \cos 2\theta & \sin 2\theta \sin\phi & -\sin 2\theta \cos\phi \\ \sin 2\theta \sin\phi & -\cos 2\theta \sin^2\phi + \cos^2\phi & (\cos 2\theta + 1)\cos\phi \sin\phi \\ -\sin 2\theta \cos\phi & (\cos 2\theta + 1)\cos\phi \sin\phi & -\cos 2\theta \cos^2\phi + \sin^2\phi \end{bmatrix},$$

where θ is PCS pitch encoder angle and ϕ is the PCS roll encoder angle. The rotation matrix brings the line of sight calculated from LOS_{PCS} parallel with the measured SCS slit-PCS angles was calculated. This rotation matrix, C, is given in Table 6.10.6.

Table 6.10.6. The direction cosine matrix, C, that brings the LOS_{PCS} coordinate system parallel to the instrument base coordinate system.

	Instrument X	Instrument Y	Instrument Z
LOS_{PCS} X	0.999412569	0.026375448	-0.021882692
LOS_{PCS} Y	-0.026974415	0.999256588	-0.027543658
LOS_{PCS} Z	0.021139948	0.028117751	0.999381056

The LOS in the spacecraft body fixed coordinate system, $LOS_{SC\,C}$, is given by the matrix product

$$LOS_{SC} = S^T IAC^T CLOS_{PCS}.$$

The superscript T indicates the standard matrix transpose. The matrix product $S^T IAC^T C$ that transforms LOS_{PCS} to LOS_{SC} is given in Table 6.10.7.

Table 6.10.7. The direction cosine matrix to transform LOS_{PCS} to LOS_{SC}

	SC X	SC Y	SC Z
LOS_{PCS} X	0.999420057	0.026738156	-0.02108889
LOS_{PCS} Y	-0.027335715	0.999217281	-0.028593972
LOS_{PCS} Z	0.020307821	0.029153871	0.999368595

6.11 Non-Linearity

Requirement

Any non-linearity in TES detectors and signal chains must be known to within 1% or better.

Method

One of the tests performed during calibration was to illuminate TES with scattered light from a 9.5 μm CO_2 laser. Despite the scatter plate, the laser shows a peak brightness temperature in excess of 4000K, a vastly stronger signal than TES will ever see on orbit.

Examination of these data show that there is, indeed, a small non-linearity in the system. However, the magnitude is below 0.01% and will have no measurable impact on TES retrievals. Thus the requirement is automatically satisfied and the issue can be safely ignored.

A full description of the method can be found in A&S DFM 441 (see Volume II).

6.12 Radiometric Calibration

Applying the complex calibration method, The calibrated target radiance, R_{tgt}, is given by:

$$R_{tgt}(\nu) = \frac{C_{tgt}(\nu) - C_{cold}(\nu)}{C_{OBRCS}(\nu) - C_{cold}(\nu)}\left[\varepsilon_{OBRCS} B(\nu, T_{OBRCS}) - B(\nu, T_{cold})\right]$$

$$R_{tgt}(\nu) \approx \frac{C_{tgt}(\nu) - C_{cold}(\nu)}{C_{OBRCS}(\nu) - C_{cold}(\nu)} B(\nu, T_{OBRCS})$$

Where C indicates the phase-aligned complex spectrum for target (*tgt*), and phase-aligned averaged spectra for the 90 K cold blackbody and OBRCS. We can assume the Planck function for the cold blackbody, $B(\nu, T_{cold})$ is negligible. We also approximate the OBRCS emissivity, ε_{OBRCS} to be 1.0, as discussed in TES A&S DFM # 504.

Phase Alignment

In order to average complex calibration spectra over different scans, (same detector, same scan direction) we have to perform the initial step of phase alignment to remove scan-to-scan integer sampling phase differences. These sampling phase differences are the result of variations in the starting points for interferogram sampling, giving optical path differences between scans. The difference in optical path between two scans is an integer multiple of the sampling distance defined by the laser fringe count. A difference in optical path between interferograms is equivalent to a linear phase difference between spectra. The spectral phases of different scans are aligned by looping through integer samples *k*, adjusting the phase by $\exp(-i2\pi k\nu/\nu_l)$ where ν is the spectral frequency and ν_l is the laser frequency, and checking for a minimum phase difference from a reference scan. Figure 6.12.1 shows an example of single scan phases before and after phase alignment.

Once calibration spectra are phase aligned and averaged, the target spectrum, cold blackbody average and OBRCS average have to be phase aligned. This is normally done using a double loop with integer samples *j* and *k* for adjusting the cold blackbody and target spectrum sampling phases relative to the OBRCS. Phases are considered aligned when the RMS of the imaginary term in the complex calibration equation above is minimized or when the phase difference between numerator and denominator in the complex calibration equation is minimized.

ST-5 Calibration Data

The data taken to assess radiometric accuracy and precision were sets of runs with views of the external blackbody set at temperature increments of 20K, the OBRCS set to 340K and the cold external (90K) blackbody. This analysis was performed mostly using ST-5

part B data, runs 509 and 513, corresponding to target temperatures of 220K and 300K. This data set was chosen, despite poor signal levels due to shear, because it was the only data taken with consistent gain settings for all views, which allows for radiometric calibration without added errors from gain uncertainties. Consistent gain settings are most important at the lower frequencies (2B1, 1B1 and 1B2 filters) where the instrument offset radiance contributes significantly to the measured signal and gain calibration errors would be non-negligible for the cold blackbody view set to a different gain from the OBRCS.

Radiometric calibration results

Brightness temperature precision and accuracy for the calibration results are summarized in Table 6.12.1 for two temperatures of the external variable blackbody, which was used as the target source with the cold (90K) blackbody and OBRCS (340K) used for calibration spectra. Radiometric calibration precision is given by the NEΔT (Noise equivalent delta temperature) for the average of the calibrated scans. NEΔT is computed by adding the NESR (Noise equivalent spectral radiance) to the Planck function for the source temperature and converting the summed radiance back to a brightness temperature. Systematic errors in the radiometric calibration are estimated using differences of the best fit to the calibrated brightness temperatures with the temperatures taken of the variable external blackbody during data collection. The numbers given in the Table 6.12.1 are spectral averages over frequencies inside the optical filter band passes. Figure 6.12.2 shows an example of averaged calibrated radiances and corresponding brightness temperature for a 220 K source.

Table 6.12.1. Estimated radiometric calibration precision (NEΔT) and systematic error for ST5 data.

Filter	Number of scans Averaged	220 K source (run 509)		300 K source (run 513)	
		NEΔT (K)	Sys. Err (K) T(extBB)-T(best fit)	NEΔT (K)	Sys. Err (K) T(extBB)-T(best fit)
2B1	36	1.27	0.84	0.58	0.30
1B1	20	0.44	0.62	0.23	0.19
1B2	20	0.49	0.83	0.24	0.23
2A1	10	1.21	-0.13	0.46	-0.24
2A4	10			2.0	-0.63
1A1	20			2.6	-0.56

Radiometric Accuracy Requirement

The requirement for radiometric accuracy is 0.5 K. For a 300 K source we meet this requirement for the 2B1, 1B1, 1B2, 2A1 filters, based on the limited cases that have been processed. For 2A4 and 1A1, our determination of accuracy may be limited by the number of scans averaged in the case reported here and we need to run more calibration cases for these source temperatures. This report will be updated as more calibration scans are processed, with the results for the remaining target source temperatures appended.

References:

TES L1B ATBD (Algorithm Theoretical Basis Document), JPL D-16479, V1.1, 10/1999.
TES DFM # 1427, "Initial assessment of radiometric accuracy", H. Worden, 6/16/2003.
TES DFM # 1438, "Comparisons of external blackbody to OBRCS with ST-5 data", H. Worden, 8/7/2003.
TES A&S DFM # 504, "Relatively small errors in calibrated brightness temperatures when OBRCS emissivity is neglected", H. Worden, 8/26/2003.

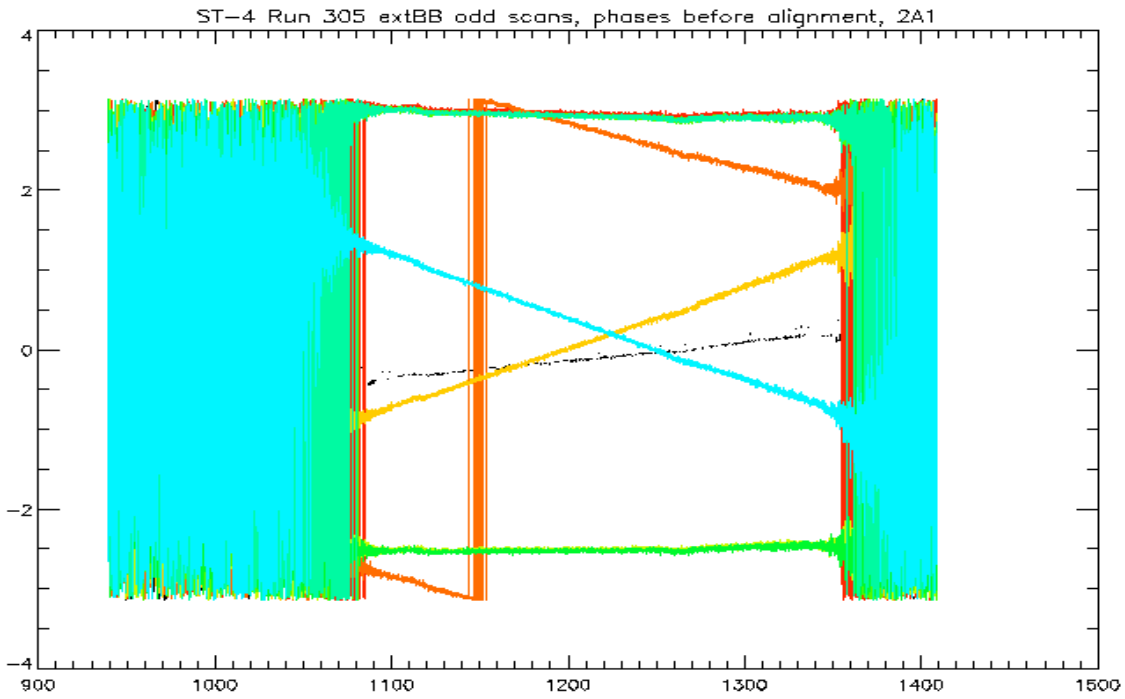

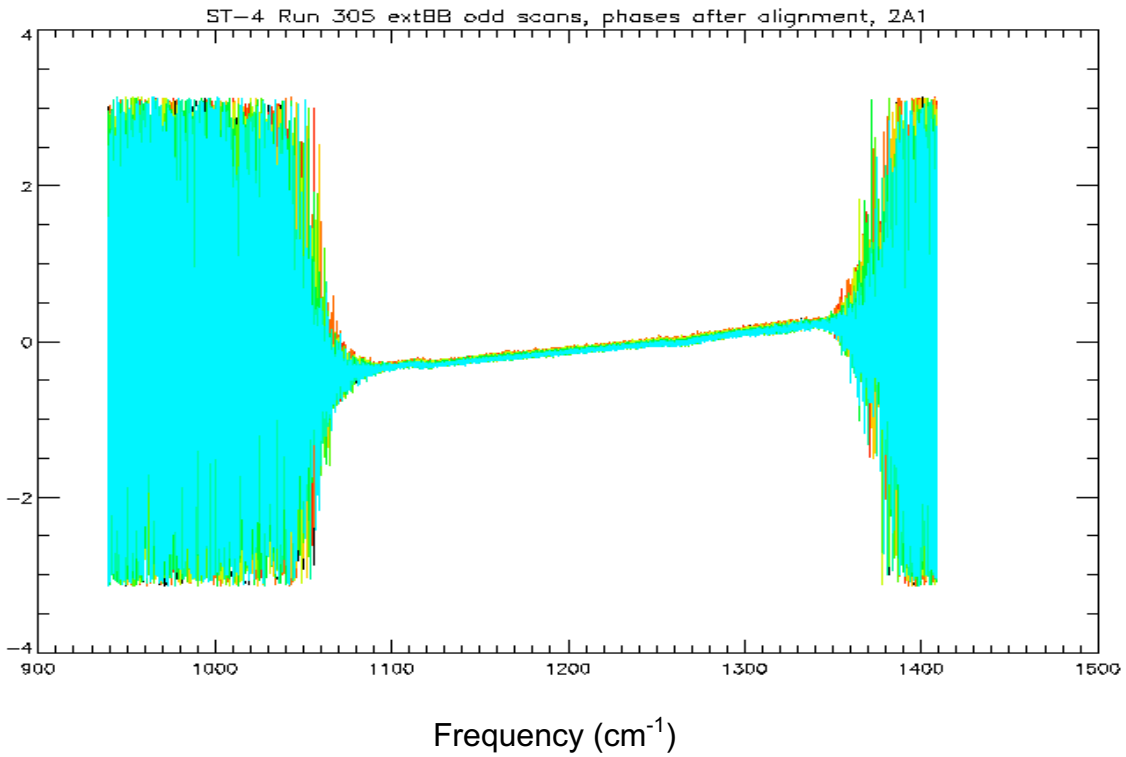

Figure 6.12.1. Example of phase alignment. Top shows the phases of individual scans before sampling phase alignment, bottom shows the phases after alignment.

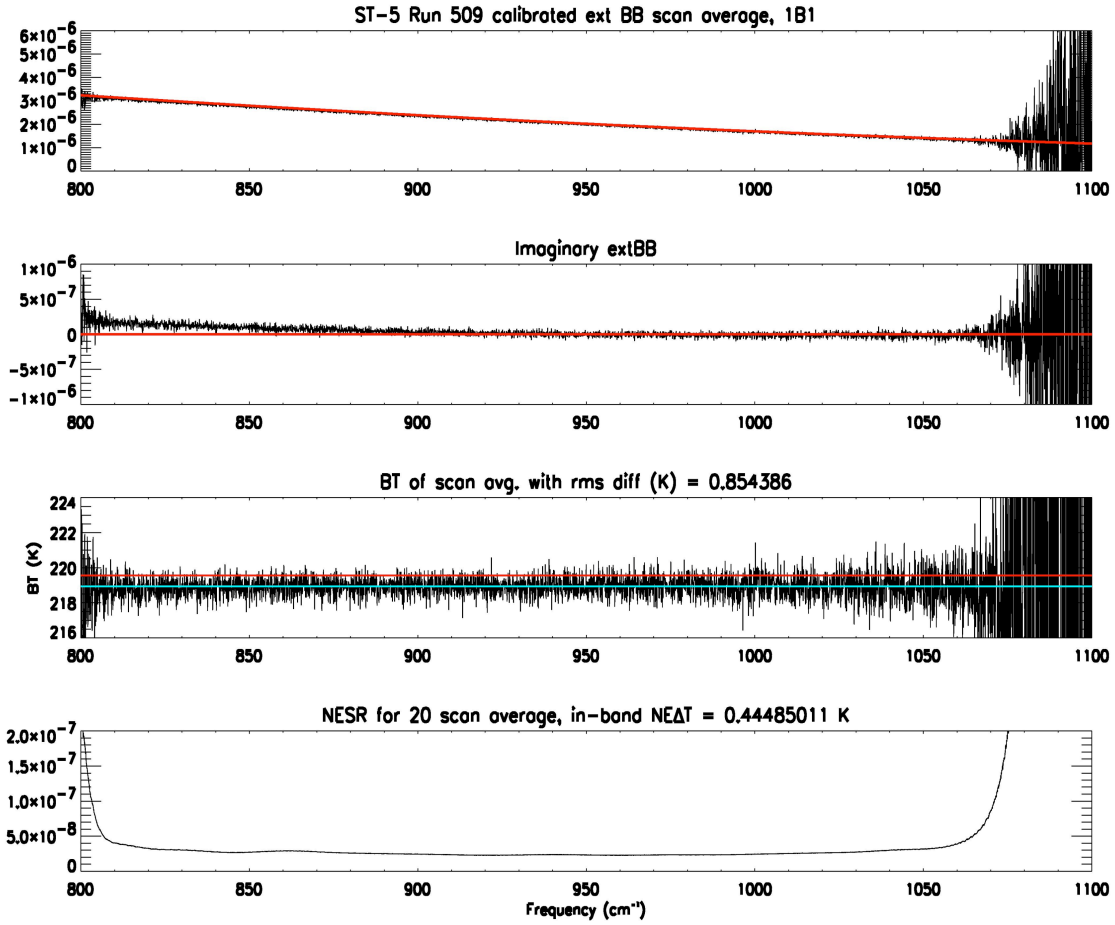

Figure 6.12.2. Example of calibrated scan average for 220 K source. The top panel shows the averaged calibrated radiance ($W/cm^2/sr/cm^{-1}$) for 20 spectra, 1B1 filter. The second panel shows the average residual radiance for the complex imaginary terms with the red line indicating zero bias. The third panel shows the calibrated radiance converted to brightness temperature and compared to the red line indicating the expected temperature for the external blackbody. The blue-green line indicates the best fit for the calibrated brightness temperature and the difference between this and the red line is the measure of systematic error for radiometric calibration. The bottom panel shows the NESR for the scan average (20 scans in this case).

6.13 NESR

Methods

Two different methods are used to estimate NESR (noise equivalent spectral radiance) from the ST-5 data. The first relies on having several spectra for the same radiometric target while the second method is used to estimate NESR for each spectrum as a part of standard L1B calibration processing.

Method 1: If several measurements of the same target (e.g., the blackbody sources from the TES system tests) are available, the NESR, by definition, is the standard deviation of the measurements at each spectral point.

Method 2: To estimate the NESR for a single radiance spectrum during complex calibration, we use the rms of the magnitude of an out-of-band spectral region:

$$\mathrm{NESR}(\nu) = \frac{\mathrm{RMS}\left|C_{tgt}(\nu_{out\_of\_band})\right|}{\sqrt{2}r(\nu)}; \quad r(\nu) = \frac{\left|C_{OBRCS}(\nu) - C_{cold}(\nu)\right|}{B(\nu, T_{OBRCS}) - B(\nu, T_{cold})}$$

where C_{tgt} is the complex target spectrum, $\nu_{out\_of\_band}$ is the frequency range for extracting the uncalibrated noise in data numbers (DN), $r(\nu)$ is the instrument response function to convert uncalibrated DN to radiance units (W/cm2/sr/cm-1) and is computed from averaged complex calibration spectra C_{OBRCS} and C_{cold} and their corresponding Planck functions $B(\nu,T_{OBRCS})$ and $B(\nu,T_{cold})$. In our case, $B(\nu,T_{cold})$ is negligible and we assume the OBRCS emissivity is 1.0.

Figure 6.13.1 shows a comparison of NESR estimates using both methods. It is important to demonstrate here that the NESR estimates using single scans agree with the statistical standard deviation of several scans of the same target since multiple scans of a stable external target, other than cold space, will not be available in orbit. Both NESR calculations are performed in the process of system test radiometric calibration, and they have consistently agreed. The in-band RMS NESR values for the two methods agree to within 2% for the cases checked, satisfying the 5% accuracy requirement for NESR measurements.

ST-5 data used for NESR estimates

Most of the NESR estimates reported here were performed using the same data set from ST-5 part B used for radiometric calibration, with significantly lower signal levels due to interferometer shear. Lower signal levels in the OBRCS data result in higher NESR values, which are less optimistic than what we expect on-orbit. However, as explained in the section on radiometric calibration, the dataset used was the only set where gain calibration errors did not have to be considered. For filter ranges at higher frequencies, exact correction of the relative gains used for data from the OBRCS view and the cold external blackbody is not as critical. Using the secondary dataset for radiometric calibration from ST-5 part A, some NESR estimates can be made for higher frequency

filters (2A1-2A4, 1A1) for cases where the gain setting used for data from the external variable blackbody was the same as the gain setting used for data from the OBRCS.

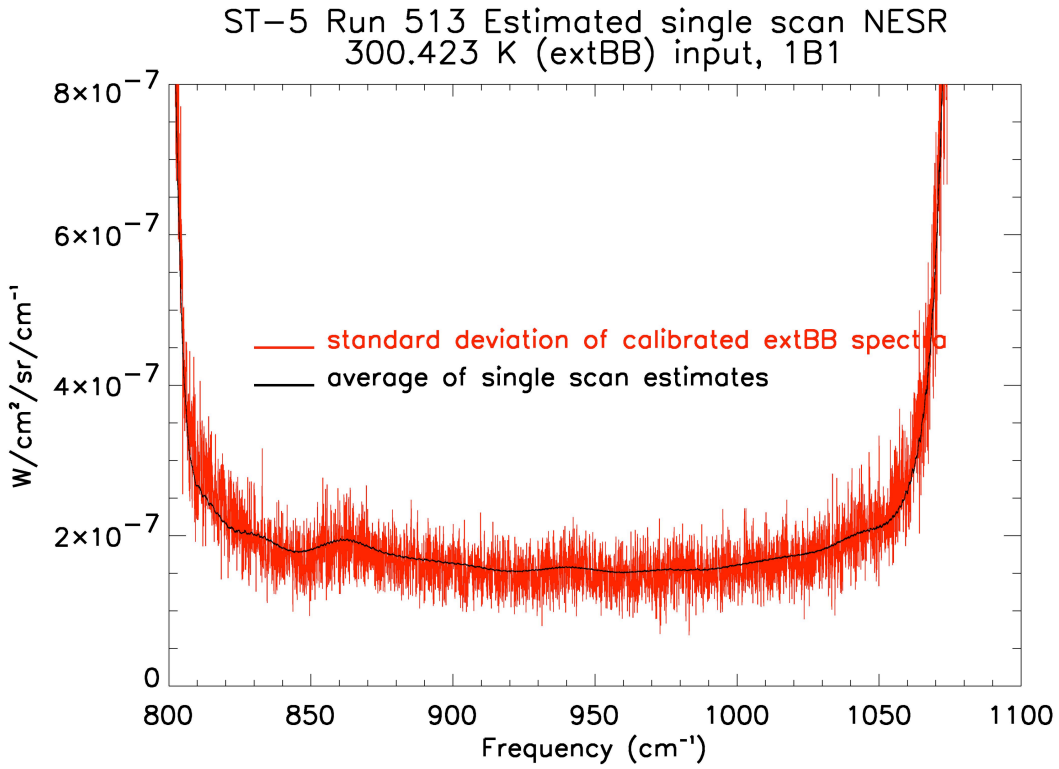

Figure 6.13.1. Comparison of NESR estimate using standard deviation of 20 scans (red) vs. estimate from calibration of out-of-band noise magnitude (black).

ST-5 NESR results

The tables below give frequency band average NESR values for the filters used in the TES global survey. Table 6.13.1 lists results from ST-5 part B runs 509 and 513, while Table 6.13.2 gives a comparison of ST-5 part A to ST-5 part B, 2A1 filter only. ST-5 part A data had significantly greater signal levels in the OBRCS magnitude spectra (about 25% larger for the 2A1 filter) compared to the part B data.

Model NESR results

The radiometric model used to predict the system signal-to-noise is described in Appendix C of the TES SOAGR (Scientific Objectives & Approach, Goals & Requirements), JPL D-11294, V6.0, 1999. The inputs to the model were adjusted so that model predictions of NESR agreed reasonably well with the ST-5 external cold (90K) measurements. Figure 6.13.2 shows the model results of NESR for limb and nadir spectral resolution at average expected source temperatures. Except for 2B1, the model NESR predictions are better than the measured ST-5 values since they assume no ice

buildup or shear. For 2B1, which is detector noise limited rather than background noise limited, the NESR value is worse because the model accounts for the average detector noise while the measurement used only detector 10, which is one of the better detectors. Limb NESR values are a factor of 2 higher than nadir due to 4 times longer integration time, however, they also have 4 times better spectral resolution.

References:
TES A&S DFM #172, "Estimating L1B NESR from single spectra", H. Worden, 11/27/2000.
TES DFM # 1329, "ST-2 NESR estimates", H. Worden, 11/13/2002.
TES A&S DFM # 492, "Measured and Predicted TES NESR for ST-5 data", H. Worden, R. Beer, 8/14/2003.

Table 6.13.1. NESR estimates from ST-5 Part B data for 4 sec scan resolution (i.e., nadir resolution). Measurements are for detector 10. NESR values are in-band averages in $nW/cm^2/sr/cm^{-1}$.

Filter	90 K Source (ext. cold BB)	220 K Source (ext. var. BB)	300 K Source (ext. var. BB)	340 K Source (OBRCS)
2B1 (650-930 cm^{-1})	590	590	640	660
1B1 (810-1060 cm^{-1})	98	110	170	200
1B2 (920-1160 cm^{-1})	100	110	170	210
2A1 (1090-1350 cm^{-1})	100	110	180	230
2A4* (1670-1980 cm^{-1})	170	Not meas.	240	330
1A1* (1890-2260 cm^{-1})	140	Not meas.	250	380

* 2A4 and 1A1 average NESR values are ~ factor of 2 worse than they would be for more optimal alignment.

Table 6.13.2. Comparison of ST-5 NESR estimates for 2A1 (pixel averages) for different shear conditions (ST-5 part A vs. part B). NESR values are in-band averages in $nW/cm^2/sr/cm^{-1}$.

Run number	90 K Source (ext. cold BB)	300 K Source (ext. var. BB)	340 K Source (OBRCS)
ST-5 part A run 458	83	142	188
ST-B part B run 513	97	191	254

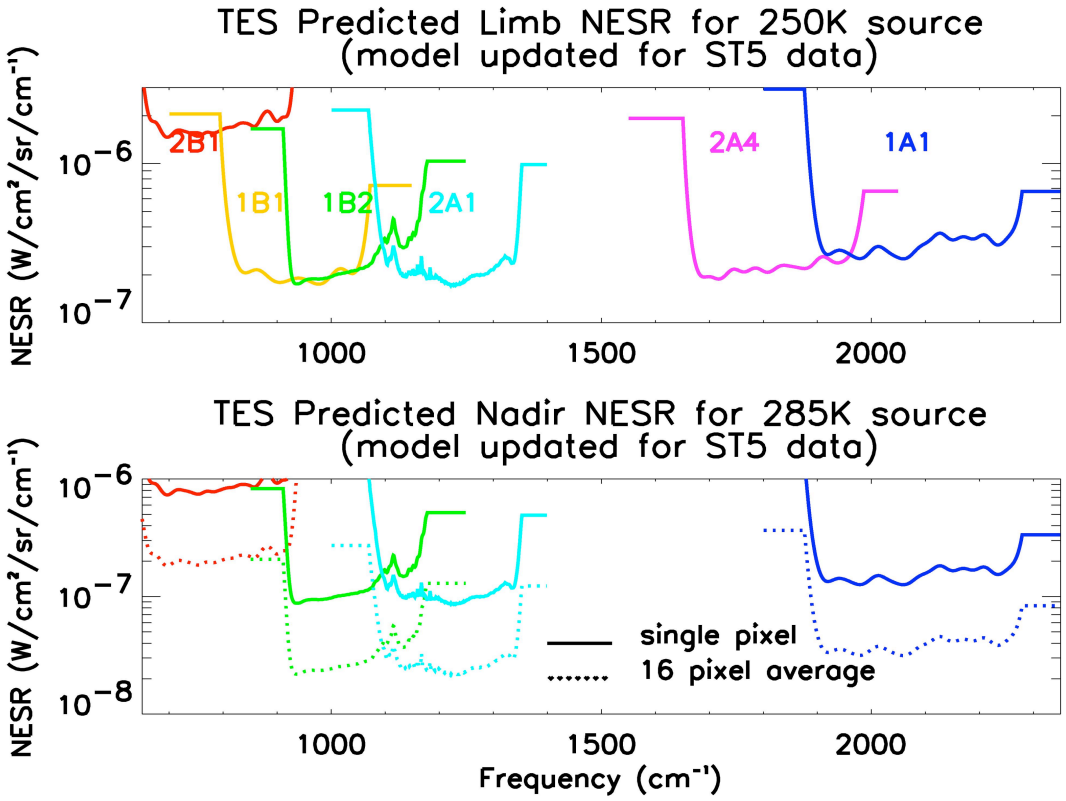

Figure 6.13.2. Model predicted NESR for optimal conditions on orbit e.g., minimal interferometer shear and no ice-buildup.

6.14 Frequency Calibration

Introduction

The SOAGR (JPL D-11204 ver. 6) lists 6 ways by which frequency errors can accumulate in TES spectra. They are:

1) All pixels are off-axis;
2) All pixels have a finite field-of-view;
3) Aberrations and diffraction modify ray paths;
4) Drifts of the control laser;
5) Interferogram sampling errors;
6) Doppler shift.

This section treats only two of them: off-axis effects and laser drifts (which are believed to be due to temperature variations of the Nd:YAG crystal). Finite field-of view (which subsumes aberrations and diffraction) appears to have only a minor effect on frequency, interferogram sampling errors are negligible and Doppler shift is analytically correctible given knowledge of the orbital velocity, pointing angle and Earth rotation.

Laser Drift

The temperature coefficient of the Nd:YAG laser is said to be –3.1 GHz/K = -0.103 cm^{-1}/K (higher temperature reduces the frequency). Given a temperature control of 0.1 K, the output frequency can change by as much as 0.01 cm^{-1}. Though it appears that this drift is reasonably slow, it is large enough that regular on-orbit frequency calibration will be necessary. Fortunately, most prominent atmospheric lines have frequencies known to a few parts in 10^{-6} cm^{-1}, which will permit more-than-adequate determination of the laser frequency.

For example, the P20 CO_2 laser line (see section 6.15.1) is located at 1046.8543 cm^{-1}. The analysis used there assumed that the Nd:YAG laser frequency was 9394.3482 cm^{-1} but the apparent CO_2 frequency was 1046.8832 cm^{-1}, from which we may directly infer that the true Nd:YAG frequency was 9394.0889 cm^{-1}. It is also worth noting that the illustration (Fig. 6.15.1.1) is a 20-scan average which took almost 6 minutes to acquire but there is no evidence (at the .001 cm^{-1} level) that there were any frequency drifts during that period.

Off-axis Effects

As was discussed in A&S DFM 467 (see V2), the predicted frequency shift $\Delta\nu(\theta)$ across a detector array is parabolic:

$$\Delta\nu(\theta) = \nu(0).\theta^2/2$$

Observations of CO_2 laser lines (see Fig. 6.14.1) and gas cells confirm this as well as providing a means of determining the location of the optic axis in the in-track direction.

Conclusion

Thus although most frequency shifts are predictable, enough uncertainty remains that frequent recalibration of the frequency scale will be necessary on orbit.

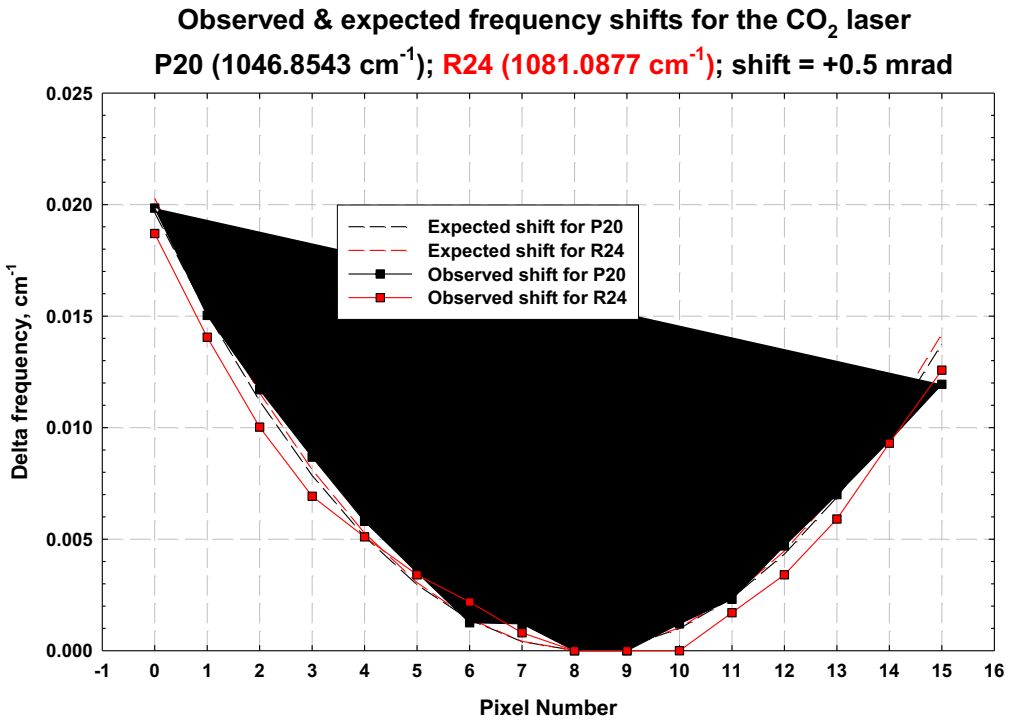

6.15 Instrument Line Shape (ILS)

6.15.1 CO_2 Laser

Introduction

During ST5, observations were made of 2 CO_2 laser lines (*via* a scatter plate to reduce the intensity to a manageable level). The lines were $00^0 1 – 02^0 0$ P20 at 1046.8543 cm $^{-1}$ and $00^0 1 – 02^0 0$ R24 at 1081.0877 cm $^{-1}$. Both lines were strong enough to provide an SNR ~1000.

Observing a monochromatic line is the most direct way of determining the instrumental line shape (ILS). ILS is a fundamental determinant of spectral quality and purity and it is essential that it be known to high accuracy in order for the retrieval process to proceed. Unfortunately, it is not a general solution because there are too few lines to cover the full TES spectral range, so the approach should be considered as a *validation* of the alternative approach which requires deconvolution of gas cell data (see Section 6.15.2).

However, the laser data are of sufficient quality that they have allowed a direct comparison of observed and predicted ILS, where the prediction is based on numerical integration of monochromatic interferograms across a field-of-view model that was, itself, based on the deconvolved IFOV data (see Section 6.16). The match is almost perfect, from which we draw the following conclusions:

1) Self-apodization can probably be ignored for all short scans;

2) Correction for self-apodization for long scans can probably be accomplished by employing a low-order polynomial amplitude function developed from the model for a central frequency for each filter together with a linear amplitude correction to the resultant spectra.

3) At the longest wavelengths (certainly 2B1 and possibly 1B1 & 1B2), no correction of any kind will be needed.

Methods

The method for producing laser spectra was straightforward – the interferograms were simply subjected to classical FSV phase correction. The result is shown as the red curve in Fig. 6.15.1.1 where the *only* manipulation done on the result was normalization to unity. In particular, note that the ILS "sits" firmly on the zero line.

The method for producing the ILS model (black curve in Fig. 6.15.1.1) is somewhat more complex. First, the mean in-track and cross-track half-widths of the deconvolved target projector FOV data were determined. From these, a response model on a 50 x 50 microradian grid was constructed for each focal plane whose in-track profile was a

gaussian of the same half-width as the measurements and gaussian ends for the cross-track response. Note that the in-track gaussians are generally wider than the cross-track ones and increase with wavelength (as expected). Fig. 6.15.1.2 shows a rendition of the model for array 1B. The response model contains 15750 bins (75 x 210).

For each bin and pixel, a cosine wave was generated according to $\cos(2\pi.\nu.\ x.\ \cos\{\theta\})$ where $\tan^2\{\theta\} = \tan^2\{\alpha\} + \tan^2\{\beta\}$ and α & β are the in-track and cross-track off-axis angles for that location, x is the optical path difference and ν is the monochromatic frequency. The result was summed across all bins after multiplication by the response model. After transformation, the ILS results (of which the black curve in Fig. 6.15.1.1 is one example).

Self-apodization

An ideal on-axis point detector in an FTS has an ILS which is the sinc function ($\sin\{x\}/x$). A (real) finite-size detector, on or off-axis, has an ILS that displays self-apodization. The ILS's in Fig. 6.15.1.1 are examples. For instance, in the sinc function the first negative lobes go to –0.22 and all the lobes are symmetric about the center. Those shown here do not quite meet these criteria. A convenient way of characterizing the departure of the ILS from a sinc function is *via* a magnitude and phase plot generated by downshifting the peak of the measured or calculated ILS to zero frequency (baseband), transforming and extracting the magnitude (= sqrt{real part^2 + imaginary part^2}) and the phase
(= $\tan^{-1}${imaginary part/real part}). Fig. 6.15.1.3 is an example (for the middle of filter 1A1 – almost the worst case).

The plots are interpreted thus:

For a sinc function, the magnitude would be identically 1 from ZPD to MPD and zero elsewhere. The phase would be zero everywhere. Since the plots of Fig. 6.15.1.3 are manifestly not of this character, they constitute *prima facie* evidence that the ILS is *not* a sinc function. Furthermore, the "droop" of the magnitude at large PD is a measure of the degree to which the secondary maxima are "sub sinc" and the non-linearity of the phase is a measure of the *asymmetry* of the ILS[1].

The magnitude can be fitted with a low-order (< 6th) polynomial which can be used to construct a function to be divided into the observed interferograms. Using a single function over an entire filter somewhat over-corrects low frequencies and under-corrects high ones but tests show that at TES OPD's and filter bandpasses, the effect is essentially linear and is easily corrected in spectrum space. Obviously, this assertion requires validation but, if it works, offers a simple way of correcting for self-apodization.

[1] A linear term in the phase is simply a measure of the shift of the data point closest to the peak from the true peak itself (and, indeed, is the basis for a powerful method of determining the true peak location)

It is also worth noting that over ranges where the magnitude "droop" is less than about 10-15%, the departure from sinc is negligible. This appears to be true for *all* short scans and for long scans at long wavelengths.

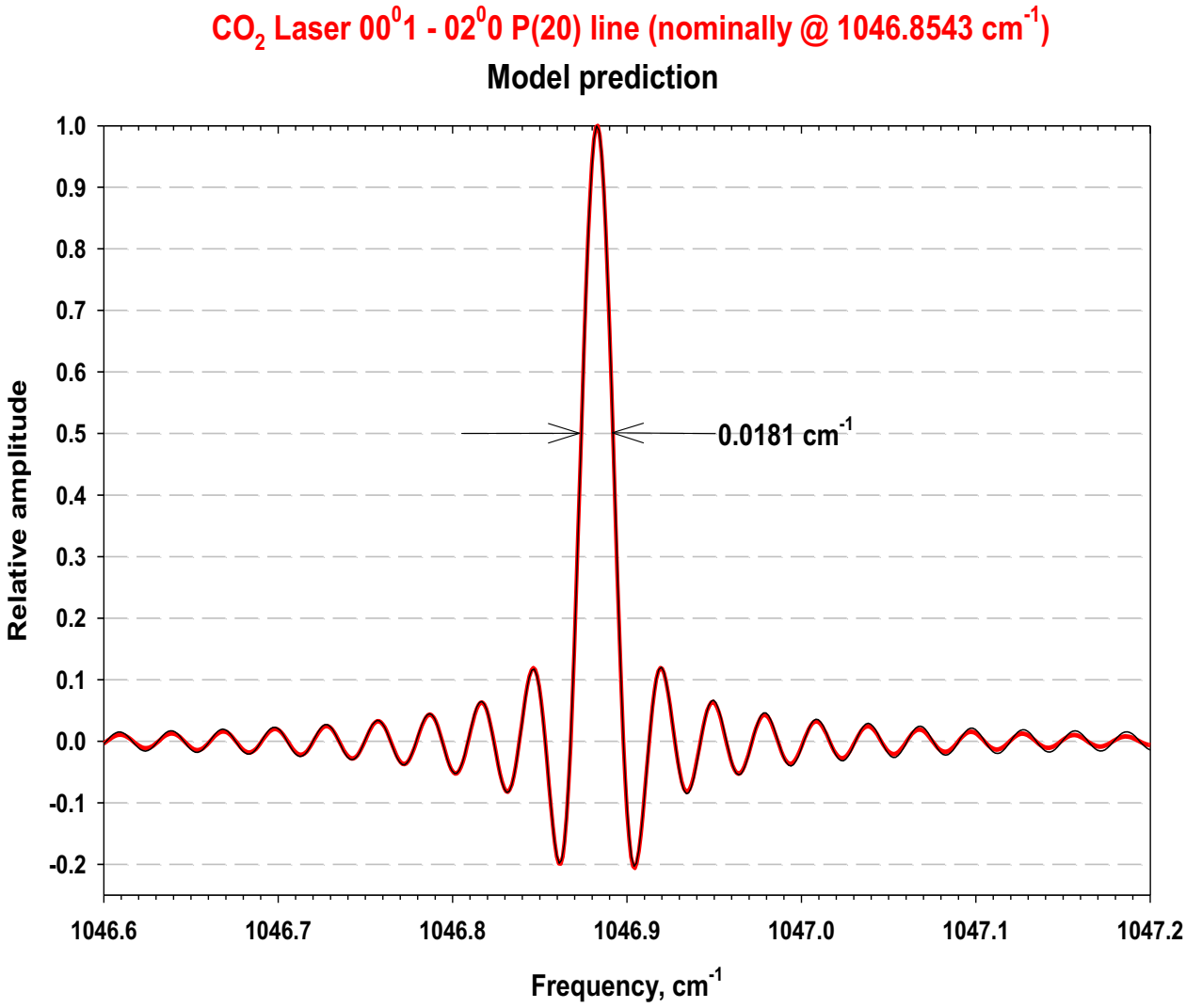

Figure 6.15.1.1: red: measured CO_2 laser line; black: predicted ILS based on a field-of view model.

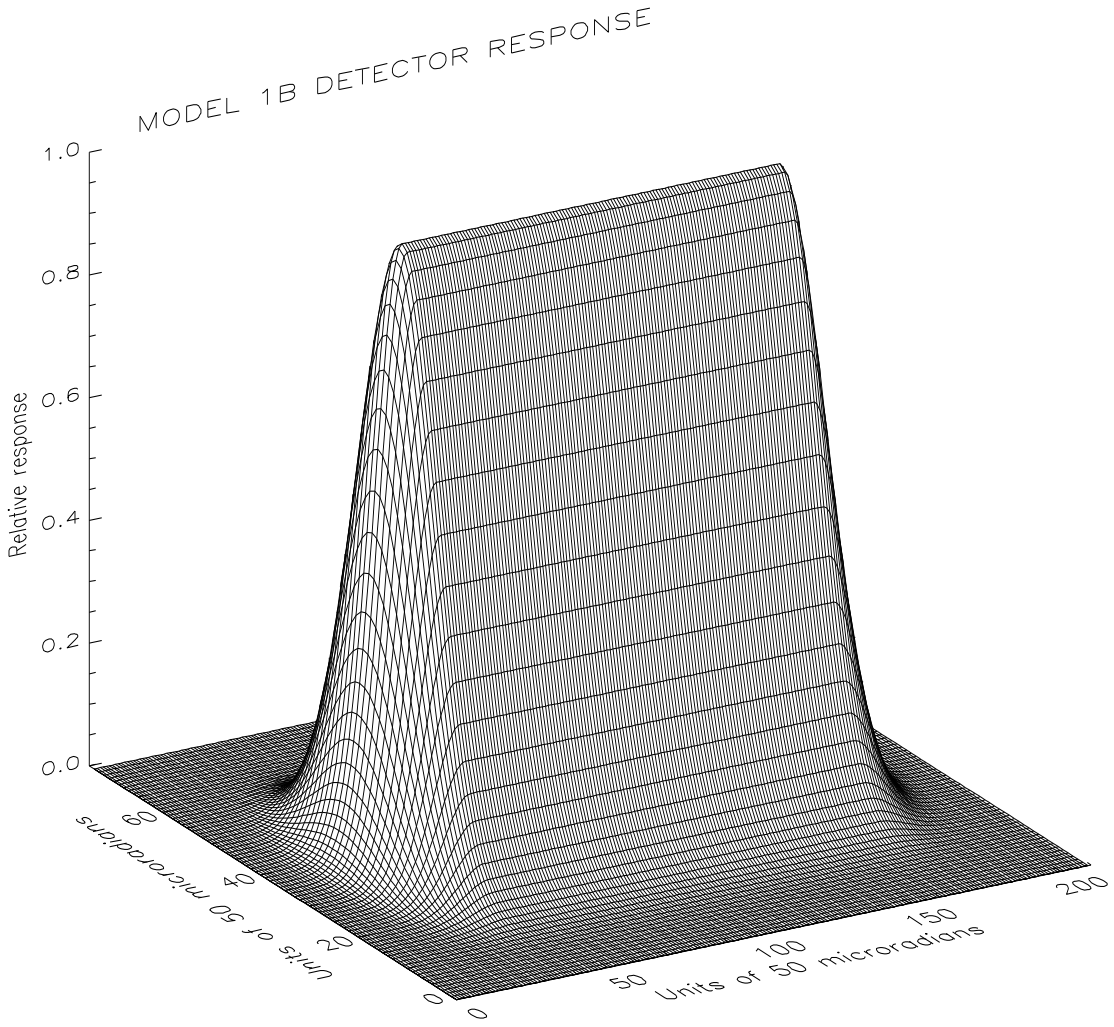

Figure 6.15.1.2: Model of the 1B array response (average for all pixels)

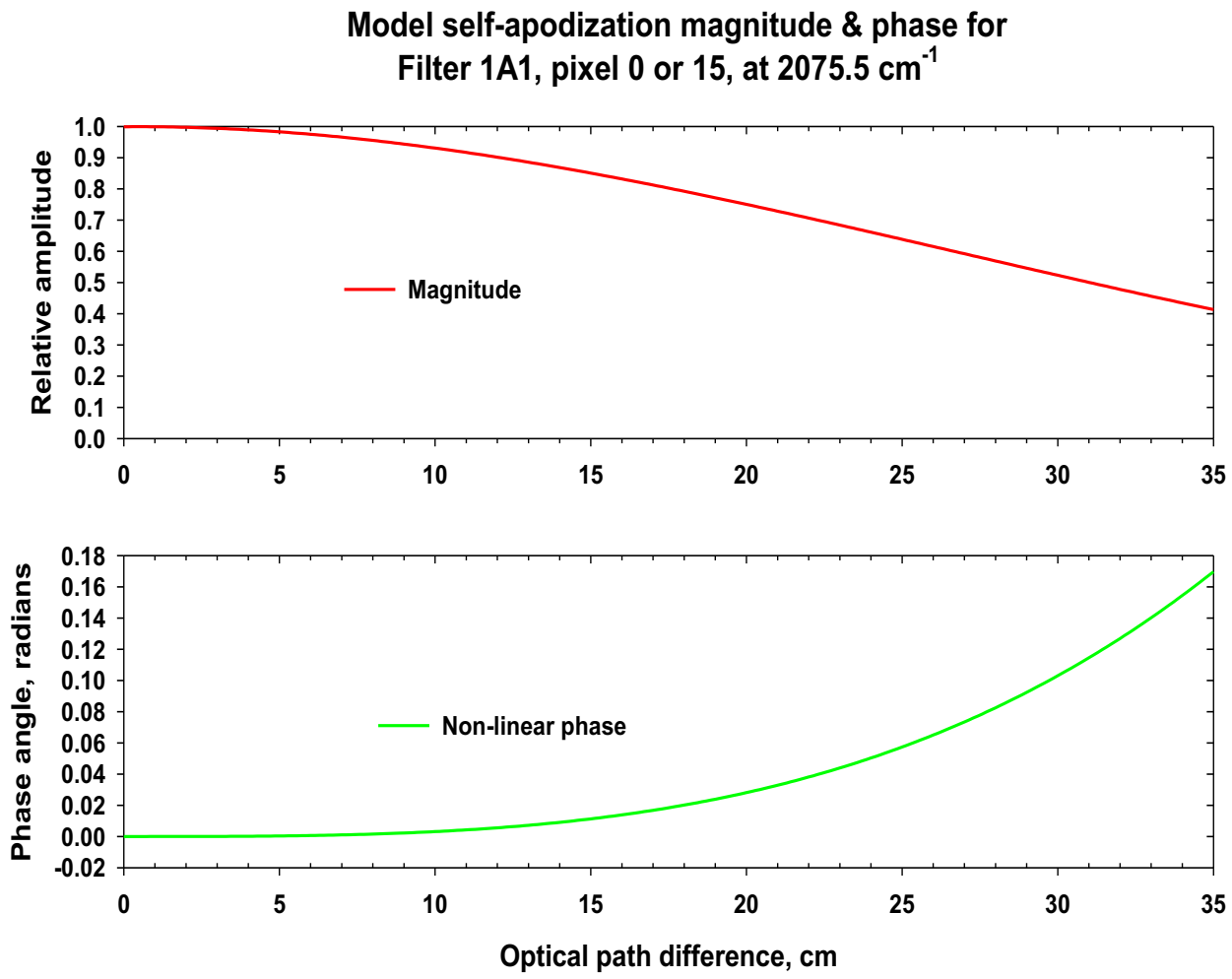

Figure 6.15.1.3: Example of self-apodization plots.

6.15.2 External Gas Cell Data

The external gas cell measurements combining with model simulations are used to spectrally characterize the instrument, including the frequency calibrations for the measured spectra and the instrument line shape. The gas cell measurements were made in TV19 interferometer only measurements, and in the integrated system tests ST1, ST2, ST4 and ST5. Table 6.15.2.1 lists the gases and the cell pressures etc. used in ST5 part A. A background blackbody at 340 K provided the radiation source. The radiation went through a 40 cm long gas cell before entering to the instrument. The gas pressures were carefully chosen for targeted filters (spectral ranges) so that the majority of the absorption lines are detectable but not saturated.

Table 6.15.2.1. ST5 – A Gas Cell Measurements

Test ID	Run Cnt	Measurement	Target Filter	Cell Temp (K)	Cell Press (Torr)	BB Temp (K)
372	461	Empty 320 K BB	1A2, 1B1,1B2, 2B1			317.6
373	462	Empty 340 K BB, OBRCS, and Cold BB	1A2, 1B1, 1B2, 2B1			336.9
374	463	CO_2 150 Torr 340 K BB	1B1, 1B2	286.7	149.8	337.1
375	464	CO_2 10 Torr 340 K BB	1A2, 2B1	288.6	10.3	336.14
376	465	Empty 320 K BB	1A2, 1B1, 1B2, 2A3, 2A4, 2B1			317.7
377	466	Empty 340 K BB, OBRCS, and Cold BB	1A2, 1B1, 1B2, 2A3, 2A4, 2B1			336.96
378	467	N_2O 150 Torr 340 K BB	1B1,1B2,2A3,2A4	290.6	150.0	336.8
379	468	N_2O 5 Torr 340 K BB	1A2, 2A1, 2A2	291.5	5.2	337.04
380	469	Empty 320 K BB	1A2, 2A1, 2A2			317.63
381	470	Empty 320 K BB	1A1			317.8
382	471	Empty 340 K BB, OBRCS, and Cold BB	1A2, 2A1, 2A2			337.0
383	472	Empty 340 K BB, OBRCS, and Cold BB	1A1			336.72
384	473	CO 5 Torr 340 K	1A1	291.8	4.9	337.13

The gas cell measurement and the empty cell measurements at two background blackbody temperatures are used to derive the measured radiances (A&S DFM 337). A gas cell model simulation (LBLRTM with HITRAN 2000) is then made to compare with the measurement. As a first step, the pixel-dependent apparent laser frequencies were retrieved from measurement-model comparison (A&S DFM 464, 337 &447). This step greatly reduced the measurement-model radiance residual.

There are a number of reasons possibly contributing to the remaining measurement-model residuals. A&S DFM 512 listed and analyzed several reasons. This DFM summarized some preliminary results from the studies on the ST5 gas cell data to assess the role of ILS on the measurement-model residuals.

Two important conclusions can be drawn from this study. First, The smaller signal to noise ratio of the instrument compared to the original prediction, due to variety of reasons including not applying electrical filter, seems to "hide" the effect of ILS on measurement-model residuals. The noises in the measured spectra dominate over the systematic errors introduced by not-well-known ILS. Second, when applying the theoretical ILS based on

the geometry of the detectors to the model radiance, the measurement-model residuals are reduced. This implies that the theoretical ILS reasonably describes the ILS for the real instrument.

6.16 Field of View (FOV) Response

The TES Field-of-View (FOV) was measured to assess both the spatial response of the pixels as well as the relative boresight between the four detector arrays. Measurements of the TES FOV were made using an external target projector equipped with a chopper. The target projector source was a slit 0.75 milliradians wide and approximately 12 milliradians long. The slit was oriented with the long dimension parallel to the long dimension of the pixels for assessing the FOV for limb scans and the relative detector alignment perpendicular to the long axis of the pixels (along track). For assessing the relative alignment along the long axis of the pixels, the slit was oriented with the long dimension perpendicular to the long dimension of the pixels(cross track). In both cases, the slit image was scanned across the array by moving the source in the target projector in a direction perpendicular to the slit long axis. A schematic diagram of the scan directions is shown in 6.16.1.

To measure the pixel response, the amplitude of the chopped signal was computed. The chopped amplitude was defined difference in the mean values of the chopper open and chopper closed phases after the zero-path-difference signal and noise spikes were removed. The resulting response curves where then used directly for boresight location. Additional details regarding relative boresight can be found in section 5.3: Shear/Co-Boresight.

For limb FOV use, the curves were further processed to remove the effects of the finite slit size and target projector diffraction. The slit and diffraction effects were deconvolved from the FOV curves using a Richardson-Lucy algorithm. More details of the deconvolution are documented in TES A&S DFM #479. Examples of the deconvolved FOV curves for each detector array are shown in figures 6.16.2 to 6.16.5.

The pixel response curve are approximately Gaussian with a broader base. The along-track full-width at half-maximum were approximately 0.75 milliradians for 1A1, with the longer wavelength filters being slightly larger due to diffraction within TES. Cross-track widths were the expected 7.5 milliradians. Inter-pixel spacing was the expected 0.75 milliradians. Full-width at half-maximum or each pixel and inter-pixel spacing are tabulated in TES DFM #1432. The arrays exhibited some variation in peak response across the pixels, which is documented in A&S DFM 498.

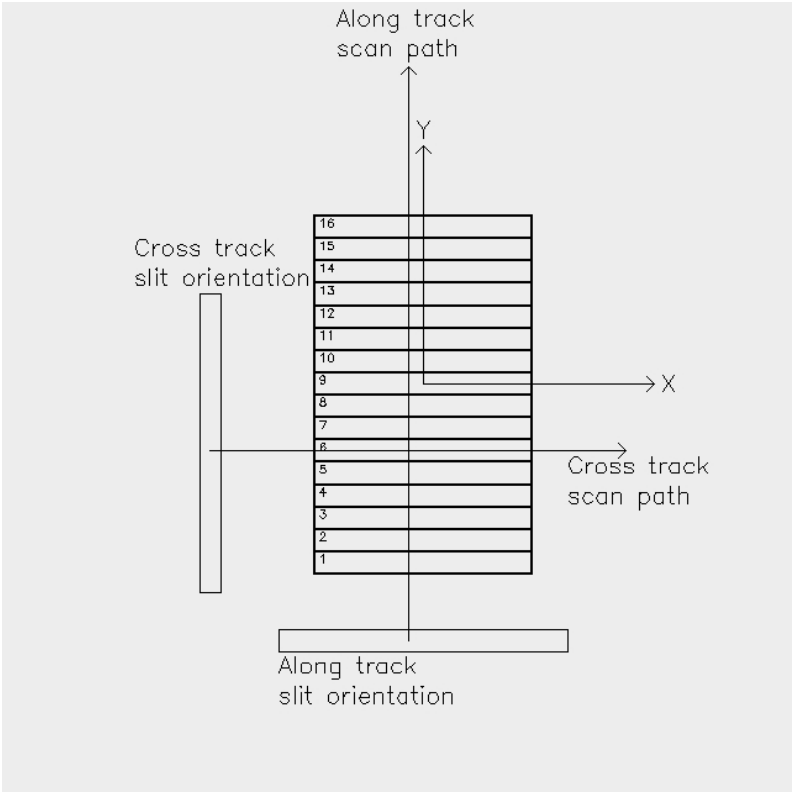

Figure 6.16.1

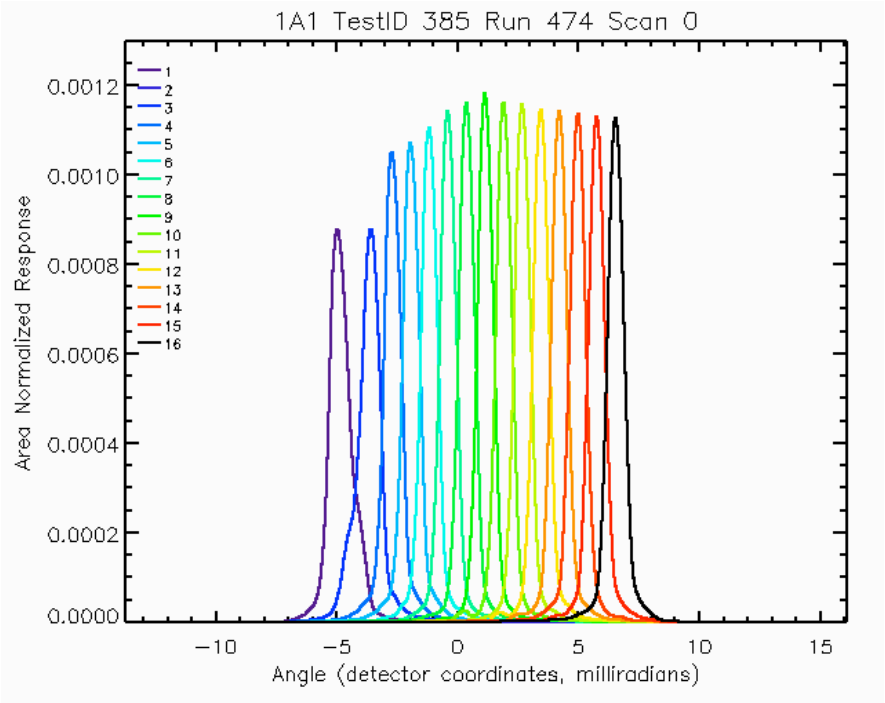

Figure 6.16.2

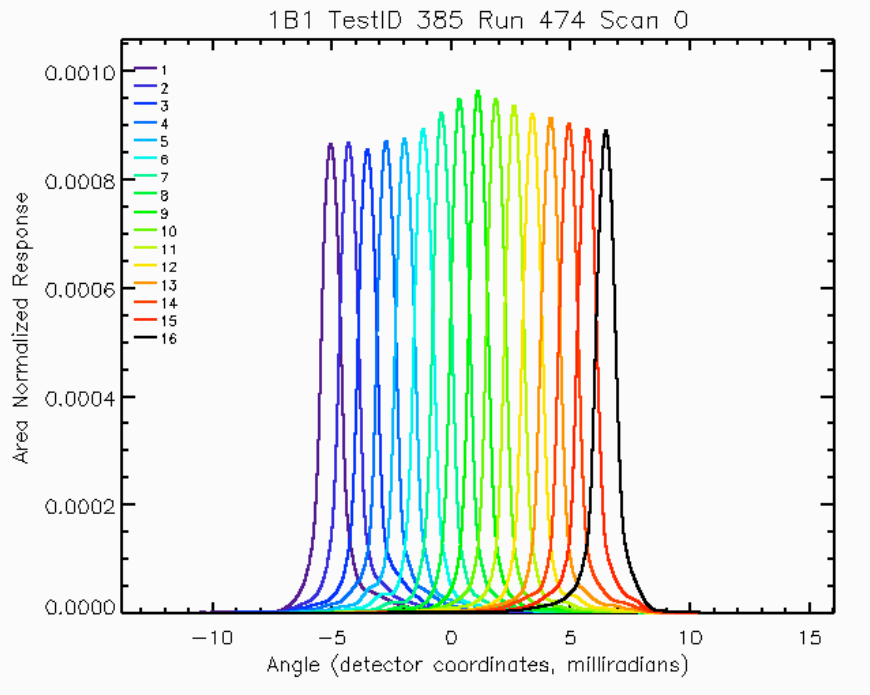

Figure 6.16.3

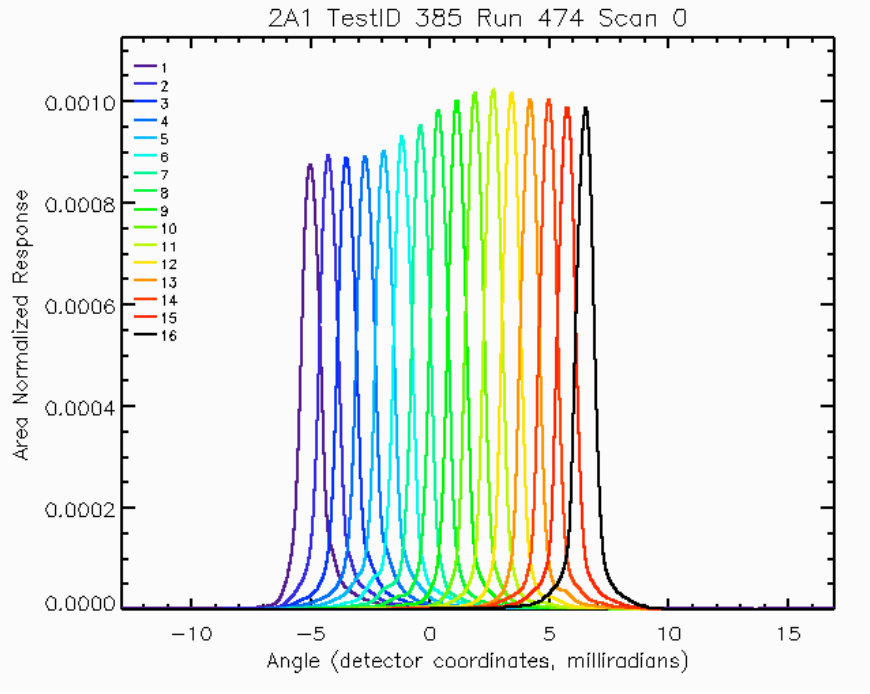

Figure 6.16.4

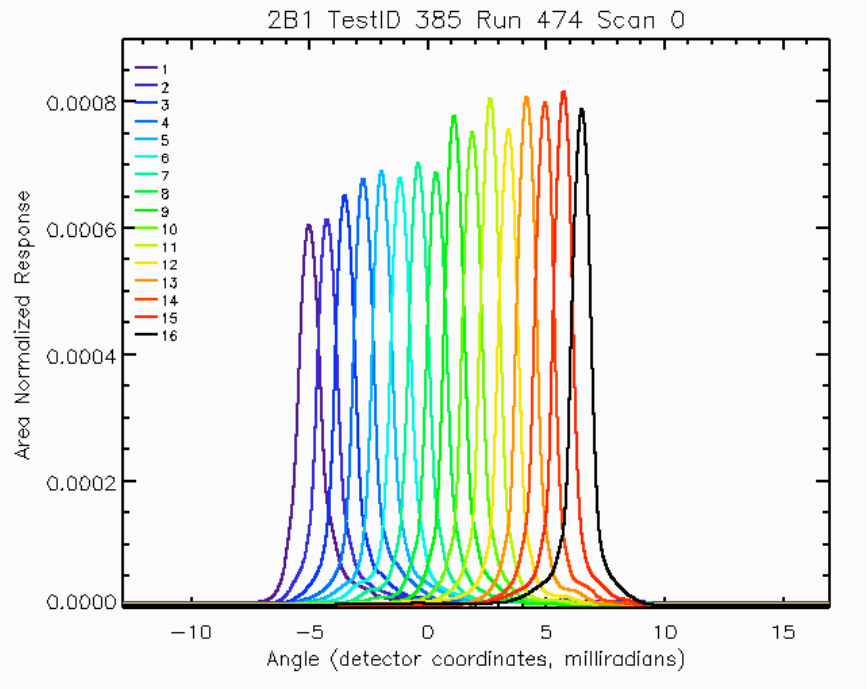
2B1 TestID 385 Run 474 Scan 0
Area Normalized Response
0.0000
0.0002
0.0004
0.0006
0.0008
1
2
3
4
5
6
7
8
9
10
11
12
13
14
15
16
−10
−5
0
5
10
15
Angle (detector coordinates, milliradians)

Figure 6.16.5

7.0 CONCLUSIONS – IMPACTS ON ALGORITHM REQUIREMENTS

The analysis of calibration data has led to a number of changes to the algorithm and software requirements. In some cases, these changes required additional algorithm requirements, e.g., the calculation of shear from spectral phase measurements, and in other cases, has led to a relaxation of requirements, e.g., the lack of non-linearity in the detector responses. Table 7.0 summarizes which subsystems are impacted by the system test findings and whether or not a new requirement was necessary.

The existence of channel shifts requires two changes to the Level 1 software and algorithm requirements. The first is the implementation of the channel detection and correction algorithm (Sec 6.1) into the L1A software. The second is a partial check of the correction in Level 1B software through analysis of the spectral phase for all detectors in a focal plane.

This latter requirement is implemented in software with the TES performance monitoring algorithms. These algorithms monitor the shear using the spectral phase of the OBRCS radiance measurements (Sec 6.3) . In addition, the time variations of the spectral signal magnitude, which is calculated in regions sensitive to ice build-up, is also monitored (Sec 6.4). Changes in shear and ice-build up both affect signal levels and therefore the signal-to-noise. If the signal levels drop below a predefined threshold, then TES personnel will be alerted and an appropriate action will be pursued, e.g., warming the detectors to remove ice.

There are several results that have no appreciable impact on Level 1B processing or algorithms. The analysis of the stability of channeling from the ST data set suggest that channeling will have no impact on system performance or L1B processing (Sec 6.5). The decision to use a single gain setting obviates the need for gain calibration (Sec 6.7). The lack of significant non-linearities in the detector response removes the need for a correction algorithm (Sec 6.12). Other results, such as the FFT sizes and spectral frequency ranges (Sec. 6.2) were needed so that default values used in the algorithm could be replaced with measured values.

The impact of the velocity variations of the interferometer arm on the spectra through the electrical filters has lead to an operational decision to turn those filters off. If a correction can be developed for the electrical filters, then a significant software development will be required in Level 1B to implement that algorithm. In the absence of correction algorithm, the NESR has been increased by over a factor of two (Sec 6.6). However, no special processing is required in that case.

There are several results of the calibration analysis that affect both Level 1B and Level 2 processing. Our standard method for calculating the NESR has been validated with the ST data (Sec 6.14). However, the increase in NESR from the predicted values requires a reevaluation of the “microwindows” selected for the Level 2 retrievals. In addition, the measured spectral spikes must also be included in the Level 2 microwindow selection

process (Sec 6.8). The time-variability of the spike frequency locations will be monitored in Level 1B. The calculation of the field-of-view (FOV) will be used to reevaluate microwindows for TES limb retrievals (Sec 6.16). In addition, the FOV is used to calculate the theoretical ILS function, which is used by both L1B and L2.

From the analysis of the ILS, no correction for the ILS will be applied in Level 1B processing or modeling of the ILS in Level 2 for nadir spectra. In the case of the limb mode and higher frequencies (>1500 cm^-1) (where the effect of the ILS is more important), additional study will be required.

Ultimately the impact of the system test characterization on the expected accuracy and precision of TES retrievals must be assessed. The One Day Test (ODT), which is currently in progress, is using the expected NESR from the system tests to assess retrieval precision and vertical resolution. The ODT simulates spectra, with added noise, and performs retrievals for nadir and limb target scenes over 16 orbits. Further retrieval studies will need to be performed that include the effects of calibration systematic errors, such as radiometric accuracy.

Table 7.0 Impacts of System Test Results on Data Processing Subsystems

System Test Result	Section Number	L1A	L1B	L2	New Requirement
Channel Shifts	6.1	X	X		Yes
FFT Size/Filter Ranges	6.2		X		No
Shear/Co-Boresight	6.3		X	X	Yes
Time Trend of Signal	6.4		X		No
Channeling Stability	6.5				No
Electrical Filter	6.6				Yes, if correction is implemented
Gain	6.7		X		No
Spectral Spikes	6.8		X		No
Cal. Pointing Angles	6.9	X			No
PCS Calibration	6.10	X			No
Non-Linearity	6.11				No
Radiometric Calibration	6.12		X	X	No
NESR	6.13		X	X	No
Frequency Calibration	6.14		X	X	No
Instr. Line Shape (ILS)	6.15		X	X	No
FOV Response	6.16		X	X	No